NUMERICAL MODELLING OF THE PROPAGATION ENVIRONMENT IN THE ATMOSPHERIC BOUNDARY LAYER OF LITTORAL AREAS

Application of the TERPEM Propagation Model

R. S. Plant and B. W. Atkinson

Department of Geography
Queen Mary and Westfield College
University of London

Contents

Abstract

The code `TERPEM` solves numerically a parabolic approximation to the wave equation and is used to predict propagation environments under ducting conditions in the Persian Gulf. It requires as input a specification of the refractivity field and this is determined from the results of a mesoscale meteorological model. Some important aspects of the transfer of data between the mesoscale model and the `TERPEM` code are considered, not least the mechanisms for interpolation of refractivity data in both the horizontal and the vertical. Some suggestions are made for improving the modelling capability of `TERPEM`. The meteorological conditions have been divided into high and low wind conditions, characterised by wind speeds in the predominant air flow from Saudi Arabia over the Gulf waters. High quality observational data is available for the days simulated by the mesoscale model and propagation within the observed and simulated refractivity environments is compared.

In the low wind case, a simple surface duct of about 100 m depth supports strong trapping of radar energy. By contrast, the duct in the high wind case is about three times as deep, but trapping within it is weaker. Within $\sim$ 100 km or so from the coast a simple surface duct also occurs in the high wind case, but further out to sea an S-shaped duct develops, the base of the trapping layer lying about 200 m above the sea surface. This development has a significant impact on propagation, particularly over paths that include a transition between the two types of duct. During the late afternoon and early evening, a sea–breeze circulation (SBC) becomes established. Movement of marine air coastwards by the SBC smooths out the horizontal gradients between the land and sea air masses and has important effects on the propagation around the coast.

Fine details of the refractivity environment, beyond the scope of a mesoscale model, are required for accurate prediction of the propagation environment. Nonetheless, the present study is encouraging. Refractivity fields provided by the mesoscale model are sufficiently detailed that some quite subtle influences on propagation can be distinguished. In many existing studies of propagation environments there are considerable uncertainties associated with forced assumptions of spatial and temporal homogeneity. It is suggested that mesoscale models offer a useful and powerful tool for interpolating in both space and time between routine observation profiles, which tend to be widely–spaced and infrequent.

1   Introduction

This project is concerned with assessing the capability of mesoscale numerical models for predicting the propagation environment in coastal areas. Phase 1 covered the testing of a non-hydrostatic, numerical model in idealised and realistic situations (Li and Atkinson, 1997a,b, 1998a,b). The realistic cases (Li and Atkinson, 1998b) were run to simulate conditions in the Persian Gulf in a period when aircraft observations had been taken (Brooks *et al.*, 1997, 1999). The results were encouraging and showed that the model was capable of capturing the essential features of the propagation environment. A marine boundary layer (MBL) over the Gulf was well simulated in both its depth and the gradients of temperature, humidity and refractivity therein. In addition to the important vertical gradients at the top of the MBL, well-developed sea-breeze circulations were found which exhibited a strong horizontal gradient at the boundary between sea and land air. It is tempting to call this gradient the sea-breeze front (SBF), but care in nomenclature is required here as observations of such fronts show them to be hundreds of metres, rather than several kilometres, wide.

In the light of the results from Phase 1 it was decided to pursue four aspects of the project: first, the effects of horizontal grid resolution on the simulations; second, a more detailed analysis of the SBF; third, horizontal variations within the MBL; fourth, the incorporation of the `TERPEM` model, a code that allows calculation of the response of electromagnetic radiation to the propagation environment produced by the meteorological model. Plant and Atkinson (1999, 2000) have discussed the effects of grid resolution (1999) and the development of the MIBL (2000). This report discusses the application of `TERPEM`.

2   Radar Propagation Modelling

The propagation of electromagnetic radiation in the atmosphere is affected by the presence of absorbing material, the distribution and nature of localized scattering centres (eg, precipitation) and the cumulative effect of scattering from the atmospheric gases, which leads to a non-trivial refractive index. Absorption of radar signals is a minor effect for most radar frequencies and is usually neglected below $\sim 1\,\mathrm{GHz}$. It can be taken into account by using the extensive data that is available for absorption rates as functions of frequency, pressure and water–vapour pressure (Bogush Jr, 1989). The effects of localized scaterrers can be very important: indeed, the study of the properties of such scatterers is a major field of application in its own right (Battan, 1973; Gossard, 1983). Here we are interested in propagation within the lowest few hundred metres over the Persian Gulf and so such scattering can safely be neglected. The refractive index of the

atmosphere can be expressed as a function of meteorological variables and is often determined by means of the semi-empirical formulation of Bean *et al.* (1970),

$$N = \frac{77.6}{T}\left(p + \frac{4810e}{T}\right). \tag{1}$$

In the above equation, N is a scaled form of the refractive index known as the refractivity ($N = 10^6(n-1)$), T is the temperature (K), p the pressure (mb) and e the water–vapour pressure (mb). The first term on the right–hand side (RHS) of Eq. 1 is simply proportional to the density of dry air. Although there is a small contribution made by carbon dioxide, the dominant part is due to the presence of oxygen, the molecules of which have a permenant magnetic dipole moment. The second term arises because at the low frequencies of radar, molecules of water vapour are able to orient their permanent electric dipole in response to changes in the electric field of a propagating wave. In this report, we shall often discuss the modified refractivity,

$$M = N + \frac{z}{R} \tag{2}$$

which is introduced in order to allow for the curvature of the earth (Collin, 1985). In this equation, z is the height above the earth's surface and R is the radius of the earth, the two quantities being expressed in the same units.

Under most atmospheric conditions, the vertical gradient of M is positive and radar signals are refracted away from the surface of the earth. However, situations can occur where M has a negative vertical gradient, at least for some range of heights. In such situations, signals can be refracted downwards towards the surface with the result that energy becomes trapped within the region of negative gradient. This phenomenon is known as ducting (Turton *et al.*, 1988) and is often associated with strong, localized vertical gradients in the meteorological variables. Ducting is known to occur frequently over the waters of the Persian Gulf (Hall, 1979; Cole, 1985; Abdul-Jauwad *et al.*, 1991), particularly during the late afternoon and early evening (Skolink, 1980). Meteorological studies of the refractivity environment in the Persian Gulf, reported by Li and Atkinson (1998b) and by Plant and Atkinson (1999, 2000), have predicted ducting conditions, the duct extending from the sea surface up to the top of an inversion in temperature and humidity that marks a marine internal boundary layer (MIBL). In the present report, we investigate radar propagation within the environment predicted by these meteorological studies.

It has long been known that propagation within a duct is well described by waveguide theory (Budden, 1961). Boundary conditions imposed by the finite extent of a guide (reflection must occur at the walls) mean that only certain, discrete modes can be propagated. The problem can therefore be reduced to that of determining the strength that is excited by the signal source in each of the modes. A generalization of the approach allows for

ducts to be analyzed in similar fashion, the width of the waveguide being replaced by the concept of a track width, the vertical distance in which a wave reverses direction. Although waveguide theory has produced many insights into ducting, it does not allow for horizontal variations of refractivity. This limits its direct practical application, since quite modest variations in refractivity can sometimes have a significant impact on propagation. Clearly the theory is not appropriate in littoral regions, in which there may be important variations in the sea-surface conditions or in which a sea-breeze circulation may produce strong horizontal gradients between sea and land air. Signals sent between sea and land may be subject to ducting for only a part of the path and are unlikely to experience uniform ducting conditions along that part.

Some of the early attempts to study the response to horizontal refractivity variations had their roots in waveguide theory. If the horizontal changes are slow then one can consider a single set of modes with weak coupling between them (Wait, 1980). However, more rapid changes really require a recognition of the effects on the modes supported. Other treatments have attempted to combine waveguide theory with ray tracing techniques (Felsen, 1981; Kukushkin and Sinitsin, 1983). More recently though, attempts have been made to solve the electromagnetic wave equation directly. The full wave equation is elliptic and thus not amenable to a straightforward numerical solution but it can be reduced to a parabolic form under a set of assumptions that are entirely reasonable when studying atmospheric ducting (scattering is taken to be purely in the foward direction and refractivity gradients are assumed to be small on the scale of a wavelength). A parabolic equation supports a marching solution and this point, together with the advent of fast Fourier transform techniques has made the approach numerically feasible. An early example is that of Dockery (1988). The success of this work, together with refinements made by other workers (see, for example, Craig (1988), Barrios (1989) and Levy (1989)), have made the approach a popular one, Dockery and Goldhirsh (1995) claiming that it is a standard method for assessing the effects of meteorological environments on naval radar applications.

This report is organized as follows. In Sec. 3 we introduce the `TERPEM` model, a computer code which solves a parabolic form of the wave equation. The operation of the code is illustrated and tested by comparing some runs with results produced by the model of Dockery (1988). In Sec. 4 refractive conditions predicted by a mesoscale meteorological model (Sec. 4.1) are used to define a ducting environment in the `TERPEM` model. The sensitivity of the propagation to radar and model parameters is studied in Sec. 4.2. The use of data from a meteorological model affords an excellent opportunity to investigate the changes in propagation conditions over time. These changes are discussed in Sec. 5 for both high and low wind conditions and for three paths with very different characterstsics. Secs. 5.1 and 5.2 consider paths

over the sea; Secs. 5.3 and 5.4 paths from a land–based transmitter looking out to sea; and, Secs. 5.5 and 5.6 paths from a transmitter over the sea to a receiver on land. In its current version, the TERPEM code limits the number of horizontal positions at which refractivity data can be provided. This means that input data to TERPEM has to be selected from the output of the mesoscale model. The implications of this, and a possible method of selection, are discussed in Sec. 6. Our conclusions are drawn in Sec. 7.

The report also includes two Appendices. These reproduce some figures from Dockery (1988) and Brooks *et al.* (1999) in order to aid the comparisons with TERPEM results that are made in Secs. 3 and 4.

3 Tests of TERPEM

TERPEM, developed by Signal Science Ltd., is a popular software package which can be used to assess the effects of the refractivity environment on radar propagation. Version 5.1 of the code (TERPEM User Guide, 1998) has been supplied to the authors of this report by the UK Met. Office. Essentially the model is designed to solve a parabolic approximation to the wave equation through the use of split–step Fourier transforms. Although there are some useful simplifications made in TERPEM in order to improve run time where conditions are favourable (Levy, 1989, 1995; TERPEM User Guide, 1998), the basic approach within the ducting region follows that of Dockery (1988). Some examples of the use of the method were provided by Dockery (1988) and are repeated here in order to check that the method has been correctly implemented into the TERPEM code.

In the examples presented by Dockery (1988), it was assumed that the sea surface was smooth: a reflectivity being set from values in the literature. TERPEM allows for a rough sea by applying a correction factor derived from the model of Miller *et al.* (1984), with an root–mean–square (RMS) wave-height taken from the saturation curve spectrum of Phillips (1966). This has been disabled for the purposes of the present tests. Although it is possible to specify a reflectivity in TERPEM no attempt has been made to exhume the data used by Dockery (1988) from the literature. Instead, the TERPEM database for sea water is used. Note also that no account was taken by Dockery (1988) of atmospheric absorption and so this aspect of the TERPEM model has been disabled in the testing.

Where the refractivity varies with horizontal distance in these examples, linear interpolation between specified profiles was made by Dockery (1988). The same approach can be adopted in TERPEM.

The first two examples use horizontal and vertical polarization of a 3 GHz antenna positioned 31 m above the surface. A sinc radiation pattern with 3° beamwidth is used. The radiation pattern corresponds to a Taylor antenna in TERPEM, although the TERPEM antenna includes only the main beam. It

would appear that Dockery (1988) included the sidelobe stucture of the antenna, which may cause some slight differences in the results. A 'standard atmosphere' (Kerr, 1951) was taken, with a constant refractivity gradient of $-39.4 \, \text{Nkm}^{-1}$. Results are given in Figs. 2 and 3 of Dockery (1988) at a height of 305 m for horizontal and vertical polarization respectively[1]. The corresponding results from TERPEM are shown in Fig. 1. As in most of this report, the radar signal strength is represented by the 1-way propagation factor, defined in the TERPEM User Guide (1998), from which the signal attenuation that would have occurred within free space has been factored out. In general the TERPEM results are in good agreement with those of Dockery (1988). In particular, the interference is less pronounced for vertical polarization since its reflection from the surface is weaker. The amplitudes of peaks and troughs do not vary so smoothly in the TERPEM results. However, to some extent this may be produced by the finite resolution that is available in the TERPEM output file (0.5 km) rather than any defect in the calculations. The spikes at the smallest ranges are not very well captured by TERPEM. However, it seems possible that the behaviour at short ranges may be subject to sidelobe effects which are not included in the TERPEM simulations.

In the third test, the antenna was raised to 1.52 km above the surface and the power as a function of altitude was plotted at a range of 5.5 km. The corresponding plot from TERPEM is shown in Fig. 2. For propagation over this short distance, with negligible surface reflection, the pattern observed is approximately that of the antenna. The main beam is reproduced correctly in Fig. 2 but obviously the sidelobes seen in Fig. 4 of Dockery (1988) are absent.

Results from the fourth and fifth tests are given in Figs. 5 and 6 of Dockery (1988). The antenna is moved back down to an altitude of 31 m, as in the first two tests[2], and the boresight is elevated by $1.5°$. The corresponding TERPEM results are given in Fig. 3. Sidelobes are again conspicuous by their absence in the upper plot of Fig. 3, but low-level interference with surface reflections is successfully captured. Similar comments to those of the first and second tests apply to the lower plot of Fig. 3. The short range behaviour differs from that reported by Dockery (1988) but the agreement at longer ranges is very good.

A surface duct is modelled by Dockery (1988) by taking a refractivity gradient of $-500 \, \text{Nkm}^{-1}$ in the lowest 37 m with a standard atmosphere above. The antenna altitude is unchanged from 31 m, but the boresight is returned to the horizontal. Strong trapping occurs within the duct. This can be seen in Fig. 4 which is in excellent agreement with Fig. 7 of Dockery

---

[1]For ease of comparison, figures from Dockery (1988) have been reproduced in Appendix A of this report.

[2]A height of 31 m is quoted in the main text of Dockery (1988) but 31 ft appears in a figure caption. Judging from the TERPEM results obtained using the two heights it would appear that metres are the correct units.

(1988). Profiles for ranges of 40, 80, 120 and 160 km are shown in Fig. 5 and should be compared to Fig. 8 of Dockery (1988). The TERPEM results at low altitudes suffer from the limited vertical resolution in the output files provided by the code, but the overall level of agreement is good.

Finally, consider the inhomogeneous duct modelled by Dockery (1988). Here the duct height increases linearly from 37 m to 150 m over a range of 100 km, with the corresponding refractivity gradient falling from $-500\,\mathrm{Nkm}^{-1}$ to $-167\,\mathrm{Nkm}^{-1}$. Conditions are uniform beyond 100 km. Results from TERPEM are shown in Figs. 6 and 7. Very good agreement has been obtained with Figs. 9 and 10 of Dockery (1988).

4   Modelling a Duct

Brooks *et al.* (1999) considered radar propagation within the Persian Gulf environment revealed by the SHAREM-115 observations. Sec. 8 of Brooks *et al.* (1999) describes modelling of a low wind day, using a code TEMPER3 which is based on a solution of the parabolic equation and hence is similar to TERPEM. In this section, we begin by investigating a similar situation to that of Brooks *et al.* (1999) but using a refractivity environment derived from a mesoscale model rather than experimental profiles. We then consider the effects on propagation of changes to the radar system parameters within the same refractivity environment.

The radar modelled by Brooks *et al.* (1999) was stated to be characteristic of a ship–mounted search radar, having an X-band frequency[3] of 10 GHz and being positioned[4] 30 m above the surface. The same values are chosen here. No other radar parameters were specified by Brooks *et al.* (1999). In the first instance we consider an omni-directional antenna with circular polarization. TERPEM 'sea-water' data are used in calculating surface reflections and all default model options are switched on (i.e., atmospheric absorption is included, hybrid integration is permitted and surface roughness is calculated using a wind speed of $5\,\mathrm{ms}^{-1}$). Refractivity data have been obtained along the mesoscale grid line $y = -54\,\mathrm{km}$ at 1400 hr on the first day of the low wind run with a 6 km grid length that was described by Plant and Atkinson (1999). The radar was placed at $x = 120\,\mathrm{km}$ and the environment between there and $x = 270\,\mathrm{km}$ was considered. The current version of the TERPEM code (TERPEM User Guide, 1998) allows for up to 10 refractivity profiles to be specified. The method for selecting these from the mesoscale model data is discussed in Sec. 6.

---

[3]Note that the same frequency was said to be typical of marine radar by Cole (1985) and Dockery and Goldhirsh (1995).

[4]Dockery and Goldhirsh (1995) took a similar value for a typical ship transmitter height, specifically 20 m.

4.1 Properties of the Duct

Duct properties along the specified line at this time are shown in Fig. 8. The duct top is defined by the highest point at which M increases with height. Not surprisingly, its growth follows a similar pattern to that of the internal boundary layer (IBL). The difference (shown in the middle plot of Fig. 8) between the refractivity at the top and bottom of the duct is approximately constant at $\sim 80\,M$-units. Turton $et\ al.$ (1988) quote a prediction of simple mode theory for the maximum wavelength that can be trapped by a duct,

$$\lambda_{\max} = C \int_0^h \sqrt{M(z) - M(h)} dz \tag{3}$$

where $C = 3.77 \times 10^{-3}$ for a surface–based duct. If the refractivity is assumed to decrease linearly within the duct then it is straightforward to derive the approximate expression given by Hall (1979),

$$\lambda_{\max} = \frac{2}{3} C h \sqrt{\Delta M} \tag{4}$$

where ΔM is the refractivity difference mentioned above. Direct integration of the mesoscale model profiles yields a somewhat lower value for $\lambda_{\max}$ (see the lower plot of Fig. 8). However, it is clear that the duct is more than strong enough to trap radiation of wavelength 3 cm, corresponding to the radar frequency used by Brooks $et\ al.$ (1999).

A plot of the one-way propagation factor obtained from TERPEM is shown in Fig. 9. The ducting is obvious, but energy trapping occurs over a slightly smaller depth (just less than 100 m) than might be predicted from Fig. 8. This is a consequence of the limited vertical resolution of the mesoscale model data that is passed to TERPEM. The results of Fig. 8 make use of interpolation between vertical mesoscale grid points according to the Chebyshev-fit method of Plant and Atkinson (2000). This produces a duct height over most of the propagation path that lies between the grid heights of 100 and 130 m. However, the refractivity profiles passed to TERPEM simply consist of a series of height–M pairs at the mesoscale grid heights. The TERPEM code makes a linear interpolation between adjacent input values. Unless the vertical resolution is very good near the top of a duct such an interpolation scheme may introduce significant inaccuracies around this turning point, especially if nearby vertical gradients are large. Ideally, such inaccuracies should be eliminated by running the mesoscale model with high vertical resolution around the duct top. In practice though this may be ruled out by numerical considerations, particularly given that the duct top over an inhomogeneous coastal region may vary from zero up to several hundred metres. That the limited vertical resolution of a mesoscale model imposes strong constraints on the ability of such models to predict detailed but important features of the propagation environment was noted by Lystad and Tjelta

10

(1995), who stated that changes in refractivity occurring on a scale of a few metres in the vertical can be of critical importance to propagation.

The effects of linear interpolation around the duct top are illustrated by Fig. 10 which compares such an interpolation to that provided by a Chebyshev fit (Plant and Atkinson, 2000). Although the fitting procedure has difficulties close to the ground, it does produce a curve which is smoother around the duct top and which has its turning point a little above the 100 m grid point. If the fit curves are used to provide more detailed refractivity data to TERPEM then there are significant differences in the results. Fig. 11 compares TERPEM results for input profiles provided by the grid point values with those obtained when the input profiles are set using 10 data points for each vertical grid point, the interpolations being made using the Chebyshev fits. The region in which energy is trapped is indeed somewhat deeper when using the smoother profile obtained from the fit. The duct also appears to capture more of the radar energy in this case. It should also be noted from Fig. 11 that there are differences in the pattern of short–scale coverage fluctuations within the duct. These fluctuations are caused by interference between waveguide modes (Joseph and Smith, 1972; Dockery and Goldhirsh, 1995) and are known to be sensitive to fine details of the refractivity environment. It is clear that the accurate prediction of this short–scale behaviour is beyond the scope of the data provided by a mesoscale model.

Returning to Fig. 9, we note that the one-way propagation factor within the ducting region decreases with height so that the duct top is not seen as a sharp transition. A decrease in the ducting strength at long range is predicted by Fig. 8 and this appears to be captured by TERPEM. Escape of energy from the duct can be clearly seen beyond ~ 80 km, which coincides with the onset of a decrease in the duct height and in ΔM. Craig (1988) has claimed that parabolic equation models are able to give a good description of such leakage, improving on the understimated rates predicted on the basis of mode theory.

A wavelike structure on the top of the duct can be seen in Fig. 9, a feature which also occurred with a homogeneous duct in Fig. 4. The streaks seen above the duct are caused by interference between a direct component and a specularly–reflected component from the sea surface. They have fixed elevation angles, although they appear to curve upwards when plotted on a rectangular co-ordinate system. The fixed angles can easily be seen on a flat–earth plot (Fig. 12). Simple geometric optics predicts that for reflection at a perfectly–conducting surface and propagation in a medium of constant refractive index, then interference between the scattered and direct rays occurs for elevation angles given by

$$\sin \alpha = \frac{n\lambda}{4h},\tag{5}$$

where h is the antenna height. Odd values of n represent destructive interef-

erence and even values represent reinforcement. This equation is valid for propagation distances long compared with h. Obviously the required conditions are not satisfied here. However, one can run TERPEM in such a uniform medium and verify that an interference pattern does occur that is correctly described by Eq. 5. Moreover, although the interference pattern can be affected by the presence of a duct (Skolink, 1980) it turns out that Eq. 5 does manage to provide a reasonable guide to the positions of the streaks in the present case. This can be seen from Fig. 13 which shows the one-way propagation factor at a height of 330 m. At this height, Eq. 5 predicts nulls at ranges of 120 km ($n = 3$), 72 km ($n = 5$) and 51.4 km ($n = 7$) and peaks at 90 km ($n = 4$), 60 km ($n = 6$) and 45 km ($n = 8$). The flat–earth plot (Fig. 12) reveals that the angles associated with cancellation from surface reflections coincide with peaks in the wavelike structure of trapping along the top of the duct. Thus, it appears that along angles of destructive interference there is less energy able to escape from the duct and therefore, just below the duct top at the same angles, there is more radar energy captured.

One can compare Fig. 9 with the coverage diagrams produced by Brooks *et al.* (1999) for a nearby path on a low wind day[5]. It is immediately apparent that the inhomogeneity in refractivity observed by Brooks *et al.* (1999) (which is taken into account in Figs. 19a and 19b of that paper) is much stronger than that predicted by the mesoscale model. It is uncertain, however, to what extent the inhomogemeity in the data used by Brooks *et al.* (1999) is genuinely caused by horizontal variations within the refractivity environment. The data were collected along a flight path of length 116 km between 0815 and 1122 UTC. Since the refractivity environment can change quite significantly over the course of three hours (as is discussed in Sec. 5), one should not regard Figs. 19a and 19b of Brooks *et al.* (1999) as predictions of the propagation environment along a certain path at some unique time. Rather those diagrams should be taken to be illustrative of the important effects on propagation that can arise as a result of inhomogeneity. Whether that inhomogeneity is spatial or temporal does not alter the thrust of Brooks *et al.*'s (1999) argument that it should be taken seriously. A more sensible basis for comparison with the general features of Fig. 9 may be provided by Figs. 19c and 19d of Brooks *et al.* (1999) in each of which a single refractivity profile is taken across the coverage region. The agreement with Fig. 19d is fairly good, the trapping depths being similar and the decrease of the propagation factor with altitude being captured towards the top of the duct. The trapping strength of the duct is perhaps a little overestimated in Fig. 9, the one-way propagation factor being slightly stronger within the duct and slightly weaker at short ranges above it. There is little evidence for escape of energy from the duct at long ranges in Figs. 19c and 19d of

---

[5]For ease of comparison, figures from Brooks *et al.* (1999) have been reproduced in Appendix B of this report.

Brooks *et al.* (1999). However, it does seem plausible that such escape may be facilitated by even a modest amount of horizontal inhomogeneity. The wavelike structure within the duct is clearly seen in the coverage diagrams of Brooks *et al.* (1999), a pattern with a wavelength of $\sim 20\,\text{km}$ occurring in Fig. 19d of that paper, as is also found in Fig. 9 here.

4.2   Varying the Radar Parameters

Now let us consider changing the radar parameters. In the example discussed above circular polarization was used. Fig. 14 shows the effects of switching to horizontal or vertical polarization. It is within the interference bands that the differences between polarizations are most noticeable. Since reflection of vertically–polarized radiation is weaker, the interference pattern is less pronounced in this case. In addition, the difference between polarizations increases with increasing range, since, as the number of surface reflections increases, the vertical component is attenuated relative to the horizontal one (Skolink, 1980). $5\,\text{dB}$ has been considered to be a reasonable error level for the predicted propagation factor (Dockery and Goldhirsh, 1995; Goldhirsh and Dockery, 1998; Brooks *et al.*, 1999). Thus, the differences between polarizations appear to be a tolerable uncertainty. Henceforth, we shall assume that the radar polarization is always circular.

Next consider the radar frequency. The results obtained using smaller frequencies of $3\,\text{GHz}$, $1\,\text{GHz}$, $300\,\text{MHz}$ and $100\,\text{MHz}$ are shown in Fig. 15. Coverage at $3\,\text{GHz}$ is similar to that at $10\,\text{GHz}$ (Fig. 9), but the wave features on the top of the duct are a little more prominent. There is also a little less structure above the duct, an observation which becomes more striking at $1\,\text{GHz}$, the interference streaks being increasingly separated as the wavelength increases. At $300\,\text{MHz}$ the waves at the top of the duct are quite pronounced and have become decoupled from the interference patterns above. Thus, although at high frequencies interference behaviour may affect these waves, they can be generated without any influence from the interference structure. Reducing the frequency further, at $100\,\text{MHz}$ ducting is no longer observed, since the wavelength of $3\,\text{m}$ exceeds the maximum value which can be supported by the duct (see Fig. 8). Nonetheless, there remains some distortion of the propagation environment, the duct leading to slightly enhanced signals at low altitudes.

Results obtained at the larger frequency of $30\,\text{GHz}$ are given in Fig. 16. The energy trapping does not appear to be as strong as in Fig. 9, the propagation factor decreasing rapidly as the range increases. This is caused by atmospheric absorption, a process which becomes important above $\sim 10\,\text{GHz}$ and which can rapidly attenutate the radar signal. Our interpretation is easily checked by switching off the `TERPEM` absorption calculation. When combined with the increased attenuation due to sea-surface roughness that applies at high frequencies, absorption imposes a maximum frequency for

practical signal transmission within a surface duct (Skolink, 1980), a feature which should be well represented by TERPEM.

Attenuation due to atmospheric absorption is fairly modest at 10 GHz, the absorption rate being $0.02\,\mathrm{dBkm}^{-1}$ for a pressure of $1000\,\mathrm{mb}$, a temperature of $25°\mathrm{C}$ and a relative humidity of 75 %. TERPEM uses three global parameters (TERPEM User Guide, 1998) in calculating the attenuation, a constant rate being applied between the source and the point of interest (see Fig. 17). This is likely to be adequate for the limited rates that occur at 10 GHz, where there is little effect from varying the parameters.

In TERPEM reflection from the sea surface is treated by applying a roughness correction factor to the standard reflection coefficient appropriate for a smooth surface. The roughness factor varies with grazing angle, wavelength and wind speed, the last of these quantities being used to estimate an RMS waveheight from the Phillips (1966) model. In low wind conditions, a value of $5\,\mathrm{ms}^{-1}$ was chosen. Setting the wind speed to zero amounts to switching off this roughness correction. Over most of the range there is little effect on the results (see Fig. 18), the propagation factor increasing slightly within the interference streaks when the roughness factor is disabled. However, there are significant differences above the duct at long ranges, more energy being able to escape from the duct when the roughness correction is applied. Thus, the wind–speed parameter is important for long range propagation. Only a single range–independent value may be set in TERPEM. For paths which lie a significant distance out to sea, this is not a handicap since it seems natural to set the parameter equal to the ambient wind speed. In general though one would like to be able to choose different values for the wind speed parameter at different ranges in order to reflect the changes within a sea breeze circulation. Moreover, for mixed land and sea paths, one needs to set this TERPEM parameter with some care. The TERPEM User Guide (1998, page 34) notes that the same method is used to determine a roughness correction over the land surface, although the treatment is not really appropriate in that case. It is hinted in the TERPEM User Guide (1998) that an enhanced treatment of roughness would be desirable in future code development. The indications from this application are that the long–range modelling capability of TERPEM could indeed be improved if such code enhancements were made.

Next we consider the choice of radar antenna. Previously, an omni-directional antenna has been used for simplicity. Another possibility is the Taylor pattern, obtained from a uniform antenna aperture. This was used in Sec. 3 for comparison with Dockery (1988). Taking a $3°$ bandwidth, which is the TERPEM default choice, gives rise to Fig. 19. The results are very similar to those obtained with the omni-directional antenna (Fig. 9) over most of the coverage diagram, although the interference pattern at large angles is suppressed because little radiation is released at such angles. The variations with changing bandwidth are as expected. A reduced bandwidth reduces

the signal above the duct, especially at short ranges, while increasing the bandwidth causes the pattern to approximate more closely that of the omni-directional antenna. Conditions within the duct are largely unaffected.

Close to the antenna beam axis, the radiation patterns of many antennas can be approximated by a suitably–chosen Gaussian form (Bogush Jr, 1989). There is little difference in the TERPEM results between a Taylor and a Gaussian antenna of the same beamwidth, the differences being comfortably below the 5 dB level referred to earlier. Since sidelobes are omitted from the Taylor pattern, the Gaussian antenna does give a wider coverage in angle resulting in higher propagation factors at the larger angles. However, the radiation at such angles is nevertheless weak.

Antennas with a $\csc^2 \theta$ pattern are often used in surveillance radar applications since (in a uniform refractivity environment) they give rise to a signal which is independent of range (Skolink, 1980; Cole, 1985). A TERPEM antenna type is available which radiates very little energy at negative elevation angles, behaves like a omni-directional antenna up to some fixed positive angle and then has the $\csc^2 \theta$ shape at larger angles. The default value for the fixed angle is $3°$ which leads to a coverage diagram similar to those of other limited–beamwidth antennas. Propagation within the duct is sensitive to radation emitted at small angles only, for which this antenna is taken to be omni-directional. The fall-off at large angles means that the interference pattern is weaker than that obtained using the omni-directional antenna. However, radiation at the largest angles exceeds that produced by a Taylor or Gaussian antenna. Although the default value for the "beamwidth" of the cosecant–squared antenna is $3°$, the TERPEM User Guide (1998) states that a value $\leq 2°$ is normal. Taking a value of $1°$ has little effect on propagation in the duct, although coverage above the duct is slightly reduced and the interference pattern at short ranges is less pronounced. However, the coverage is significantly affected if the beamwidth angle is smaller than θ_c, the maximum angle of emission for trapping within a duct (Battan, 1973; Hall, 1979; Collin, 1985), which is given by

$$\sin \theta_c = \sqrt{2 \delta M \, 10^{-6}} \qquad (6)$$

where δM is the increase in M between the transmitter height and the duct top. $\theta_c \approx 0.7°$ in the present case. Using a cosecant–squared beamwidth of $0.1°$ produces the coverage diagram shown in Fig. 20. The coverage is weaker in general since less radiation is emitted. The reduction is less strong within the duct itself, but conditions within the duct become more sporadic, the wavelike pattern noted earlier being more pronounced.

For antenna types other than the omni-directional it is also necessary to select an elevation angle. Previously the boresight was set to be horizontal. For a small positive elevation angle, the results are little altered provided that a significant amount of radiation is emitted below the critical ducting

15

angle θ_c. The interference pattern is perturbed by the change of angle, but this pattern is in any event weak for an antenna with a gain that falls off rapidly with angle. Using a $3°$ bandwidth Gaussian antenna with an elevation angle of $5°$ or above, the duct was found to have very little effect on the signal since there is little radiation that is emitted into the ducting region.

The detailed coverage within a duct is well known to be highly sensitive to the antenna height (Joseph and Smith, 1972; Dockery and Goldhirsh, 1995). This is illustrated by Fig. 21 which shows the coverage diagrams for antenna heights of 10 m and 50 m. As would be expected from Eq. 5, the streaks of the interference pattern above the duct are more widely spaced out for smaller antenna heights. The duct coverage is found to be less homogeneous with a lower antenna. The overall vertical gradient of the propagation factor across the duct increases as the antenna height decreases, indicating enhanced coverage near the surface and reduced coverage towards the top of the duct.

If one places the antenna around the top of the duct, at 100 m, then ducting is very much weaker and is very uneven. The upper plot of Fig. 22 gives the results in this case. There is a limited amount of energy trapping, mainly at ranges less than ~ 100 km. The duct appears to concentrate the signal in a band, the altitude of which has a definite wavelike variation. If the antenna is placed well above the duct (eg, at 200 m in the lower plot of Fig. 22) then there is little indication of the duct on the coverage diagram. At the longer ranges, the angles made by radiation striking the top of the duct may be shallow enough such that the duct acts as a partial barrier to the radiation. Thus, the propagation factor within the duct tends to be a little lower and that just above the duct tends to be a little larger than would have been the case with no duct present.

5   Propagation Environment Under Modelled Conditions

Having checked that the `TERPEM` code is able to produce reasonable results (Sec. 3) and having examined the sensitivity of ducting properties to the `TERPEM` model parameters (Sec. 4.2) we are now in a position to select a fixed set of parameters with which to investigate further the refractivity environments predicted by the mesoscale model. The `TERPEM` parameters and options to be used are as follows:

- A frequency of 10 GHz as in Brooks *et al.* (1999). This has a wavelength which is small enough to be captured by any practical duct. As was found by Brooks *et al.* (1999), results at smaller frequencies are similar, at least down to ~ 1 GHz. Ducting phenomena are generally

treated as potentially important when studying the propagation of frequencies above this value (Hall, 1979). At smaller frequencies, a duct may no longer trap radiation. At frequencies above $\sim 10\,\text{GHz}$, absorption by atmospheric gases becomes important, limiting the range of strong propagation to less than the 100 km or so that is considered here.

- An omni-directional antenna. Other choices of antenna would produce similar results within the ducting region provided that the gain is approximately constant within a degree or so of the horizontal. Use of an omni-directional antenna will overestimate the coverage at large angles in comparison with a practical radar system. However, our choice avoids the need to consider effects that are due to the orientation of the main beam and is commonly made in assessments of the propagation environment (Barrios, 1989; Paulus, 1989).

- If the antenna is over the sea then it is placed at 30 m above the surface as in Brooks *et al.* (1999). This puts the antenna well within the ducting region. Note that the choice of an omni-directional antenna means that the general properties of the results should not be too sensitive to the antenna height, given that a value within the duct is chosen. A land–based antenna is often placed a little lower and so we have used 20 m in this case, as in the work of Rogers (1995) and Lystad and Tjelta (1995).

- Circular polarization. In practical applications a linear polarization tends to be preferred since it is simpler to produce (Skolink, 1980). The choice of polarization does not have a great deal of effect on the results obtained. We use circularly–polarized radar because the results are then intermediate between those that would be obtained with horizontal and vertical polarizations.

- `TERPEM` data for 'sea water' (TERPEM User Guide, 1998) is used in calculating reflection from the sea surface.

- `TERPEM` data for 'very dry ground' (TERPEM User Guide, 1998) is used in calculating reflection from the land.

- Atmospheric absorption is included. The parameters used in the absorption calculation are a pressure of 1000 mb, a temperature of 25°C and a relative humidity of 75 %. This gives an modest absorption rate, which is not sensitive to the parameter choice.

- Surface roughness is calculated using a wind speed of $5\,\text{ms}^{-1}$ in the low wind cases and $15\,\text{ms}^{-1}$ in the high wind cases. As discussed above, within the sea breeze circulation and over land, smaller values for the

effective wind speed might be appropriate. Use of the ambient wind speeds will thus produce something of an overestimate of the amount of energy that escapes from the duct, a point which may be important at long range.

An important issue when using measured refractivity data to assess the propagation environment is the frequency with which recordings are made. As pointed out by Rogers (1995), the implications of uncertainties in the measurement process may be less significant than the assumption that conditions do not vary in time over a 12 hour period. The ability to study conditions at any time of interest is therefore one of the most attractive arguments in favour of the use of a mesoscale model. Changes in the propagation environment over time are discussed below, considering three different paths. All of the paths lie along the grid line $y = -54$ km, which passes over land from the western model boundary up to $x = -99$ km and over the sea thereafter. A sea–sea path was examined from $x = 120 \rightarrow 270$ km, a land–sea path from $x = -120 \rightarrow 80$ km and a sea–land path from $x = 80 \rightarrow -120$ km. The refractivity data are taken from the high and low wind runs with 6 km grid length that were described by Plant and Atkinson (1999).

5.1   Sea–Sea Path in Low Winds

Coverage diagrams at various times are shown in Fig. 23. The ducting properties and propagation conditions along the path at 1400 hr on the first day were discussed in Sec. 4.1. Strong trapping occurs below about 100 m with a wavelike pattern along the top of the layer. In the late afternoon and early evening the trapping layer decreases in height to ~ 60 m at 1800 hr due to increased subsidence as the sea breeze circulation (SBC) becomes stronger. The SBC decays during the night and the front moves inland. At 0200 hr for instance, the trapping depth increases (since the subsidence decreases) along the path as one moves through the tail of what remains of the SBC. Horizontal waves within the duct are particularly strong at this time. The depth of the trapping layer increases during the night, reaching ~ 150 m, a value maintained during the second day until the SBC starts to become strong in the late afternoon. The increased depth of the marine boundary layer on the second day has been noted previously (Li and Atkinson, 1998b). Due to a tightening of the refractivity gradient at the top of the MIBL, the signal trapping is also somewhat stronger on the second day and the signal within the duct is more uniform in the vertical direction.

5.2   Sea–Sea Path in High Winds

The duct parameters at 1400 hr on the first day, along the line $y = -54$ km are plotted in Fig. 24. In accordance with the low wind case (Sec. 4.1), the duct deepens smoothly with increasing fetch and its height is similar

to that of the MIBL. At short fetches the modified refractivity decreases throughout the duct depth. This corresponds to a simple surface duct in the classification scheme of Turton *et al.* (1988) (it is illustrated in Fig. 4a of that reference). However, at larger fetches the near–surface refractivity has a positive gradient below a trapping layer. The positive gradients are not strong enough for the duct to become elevated and the resulting configuration is referred to as an S-shaped duct (Turton *et al.*, 1988, Fig. 4b). Once this pattern has been established, the depth of the trapping layer remains almost constant at $\sim 160\,\mathrm{m}$.

The refractivity difference across the duct is about half as strong as that in the low wind case (compare the middle plots of Figs. 8 and 24). At short fetches, the refractivity at the duct top increases rapidly with fetch relative to that near the sea surface, and thus ΔM increases with increasing fetch. By contrast, at the largest fetches, after the duct height has reached a fairly steady value, the refractivity around the duct top remains constant but that between the sea surface and the trapping–layer base continues to increase somewhat with fetch. This results in a decrease in ΔM at large fetches. Plant and Atkinson (2000) discussed in some detail a perturbation to the pattern of MIBL growth, albeit concentrating on results from $1500\,\mathrm{hr}$ for a slightly–different high wind run to that considered here. A rapid rise of the top of the potential–temperature inversion was observed just behind the sea–breeze front and is believed to be caused by an interaction between the SBC and the MIBL growth mechanism. This rise is associated with relatively small jumps upwards of the isolines of refractivity (Plant and Atkinson, 1999, 2000). Although no such perturbation is apparent in the development of the duct depth, the evolution of the refractivity difference ΔM does appear to be connected to the SBC. The local maximum of ΔM in the middle plot of Fig. 24 is located close to the sea–breeze front. ΔM decreases to a minimum within the SBC, increasing again once the S-shaped duct is formed. Thus, it appears that the MIBL perturbation described by Plant and Atkinson (2000) may have implications for the propagation environment but that these may be realized in a slightly unexpected manner.

Fig. 25 gives a selection of coverage diagrams for paths over the sea. At $1400\,\mathrm{hr}$, the presence of ducting is clear. However, the variations of the propagation factor within the duct are quite unlike those seen in the low wind case. Over the first part of the path, trapping occurs across the refractivity inversion, with the trapping base at $\sim 300\,\mathrm{m}$. This is somewhat larger than the $\sim 230\,\mathrm{m}$ predicted by Fig. 24 and suggests, not implausibly, that the negative M gradient between ~ 230 and $\sim 300\,\mathrm{m}$ is small so that the ability to trap signals at these heights is considerably weaker than in the stronger gradients between ~ 300 and $\sim 400\,\mathrm{m}$. At the shortest ranges, the angles at which energy must be emitted to reach the trapping layer are larger than the minimum trapping angle for the duct. Thus, the only effect of the duct at ranges $\lesssim 35\,\mathrm{km}$ is a distortion of the pattern of interference

with sea-surface reflections. The range beyond which energy can actually be trapped within the trapping layer can be estimated from

$$\sqrt{2\delta M\, 10^{-6}} \approx h/R \tag{7}$$

where h is the height of the trapping layer and R is the range. This equation is consistent with the diagrams of Fig. 25, confirming the interpretation. After trapping has become established the base of the trapping layer acts as an absorbing surface for propagation in the lower part of the duct, and so interference streaks are restricted to the region below the trapping layer. Beyond ranges of ~ 80 km, the value of ΔM begins to decrease (see the middle plot of Fig. 24), behaviour associated with negative horizontal gradients in the isolines of modified refractivity. This has two important effects on the radar coverage. First, the minimum of M at the top of the duct is smoothed out so that gradients near the very top of the duct are somewhat weaker. Although signal trapping is maintained up to ~ 400 m a negative vertical gradient in the propagation factor develops towards the top of the duct. The second, and more dramatic effect, is the extension downwards of the region of strong radar signal, signal trapping occurring over the full duct depth beyond a range of ~ 120 km. This occurs because the track width has to be extended downwards in order to satisfy the condition for waveguide modes within the duct (Budden, 1961),

$$\int_{z_{0L}}^{z_{0U}} dz \sqrt{\mu^2(z) - \mu^2(0)\cos^2\psi} = \frac{1}{2}\lambda\left(n - \frac{1}{2}\right) \tag{8}$$

where:

- z_{0L} and z_{0U} denote the base and top of the region of trapped radar signal respectively;

- $\mu = 10^{-6}M$;

- ψ is the angle between the wave normal and the x-axis; and,

- n lables the waveguide modes.

The expression holds only when z_{0L} and z_{0U} are significantly different from the surface and the top of the duct respectively, but it should give a reasonable guide to the situation over most of the range between 80 and 120 km. As ΔM decreases so must the contribution from the trapping layer to the integral on the left–hand side (LHS) of Eq. 8. Thus, z_{0L} must decrease for the LHS to maintain the same value.

A similar pattern of coverage persists throughout the afternoon of the first day, although the duct height increases slowly throughout. Also, the development of the pattern as a function of range gradually becomes slower, as indicated for example by an increase in the range at which the region of

trapped radar signal reaches down to the surface. As in the low wind case, the duct height is considerably reduced in the early evening, but the basic features of the coverage pattern can be seen as late as 2200 hr. By midnight, however, the low–level ducting environment has been eroded sufficiently for the duct to change its character from an S-shaped surface duct into a weak elevated duct (Turton *et al.*, 1988, Fig. 4c). This leads to a modest signal enhancement around ~ 250 m with a radar hole at long ranges below ~ 200 m. During the early hours of the second day, the mesoscale model appears to break down. Although the code ran to completion through to the second afternoon, the results obtained are clearly unrealistic at that time (Fig. 26). Ducting is almost completely lost by about 0400 hr and is never recovered in this model run. The break down of model runs for the high wind case during the night has been described previously by Li and Atkinson (1998b) and by Plant and Atkinson (1999).

5.3   Land–Sea Path in Low Winds

We now consider paths from a land–based transmitter (21 km inland) looking out to sea. Coverage diagrams are given in Fig. 27. As the radar signal propagates over the sea, a duct with strong trapping properties gradually becomes established. At 1400 hr on the first day, the duct depth is just under 100 m, in agreement with the results of Sec. 5.1. There is a pronounced decrease in the propagation factor with height across the mature duct. Obviously the lower the height considered the shorter the minimum range at which radar power can be captured by the evolving duct. Thus, the vertical gradient of the propagation factor is presumably related to the development of the duct with range and suggests that the detailed mechanism of MIBL growth may be an important factor in determining the vertical signal distribution within the duct, even at long range. As noted in the discussion of sea–sea paths in low winds (Sec. 5.1), there is a horizontal wavelike pattern within the duct. Also, in the late afternoon and early evening the trapping depth falls. However, the movement of the SBF inland brings marine air landwards and thus facilitates more efficient trapping at shorter ranges. Thus, the propagation factor within the duct at 2000 hr is greater than that at 1400 hr and is more uniform as a function of height. It is interesting to note the behaviour of the leakage from the duct at this time. The propagation factor immediately above the duct is very small but increased values are observed at a height of 100 m at ranges between ~ 40 and ~ 100 km. Such an increase can be accounted for by mode theory (Budden, 1961, p. 216) which allows a wave to escape from a trapping layer by a method analogous to quantum–mechanical tunnelling. Over most of the night, there is little change in the coverage, although the duct does become more leaky with a noticeable fall-off of signal strength within the duct at the larger ranges. This is illustrated by the coverage diagram for 0200 hr. As seen for the

21

sea–sea path there is an increase in trapping depth with range at this time, albeit a modest one. Having remained at a steady value since early evening, the duct depth increases in the early hours of the morning. From about 1000 hr on the second day, a definite MIBL becomes apparent and by this time the duct has almost reached its maximum mid-afternoon depth.

A coverage diagram for 1400 hr on the second day can be seen in Fig. 27. The wavelike patterns within the duct are stronger on the second day than the first, resulting in more patchy ducts. Such waves also seem to have the effect of smoothing out much of the decrease in propagation factor with height that was seen on the first day.

5.4 Land–Sea Path in High Winds

Coverage digrams looking out to sea under high–wind conditions can be seen in Fig. 28. At short ranges, there is little evidence of trapping by the evolving MIBL. At 1000 hr for instance, trapping first becomes noticeable around 80 km. At this stage there is some indication of trapping over the lowest 200 m or so but it is strongest between ~ 150 and 200 m. This corresponds to the trapping layer of the S-shaped duct that comes into being at that range and is due the strong refractivity gradients across the inversion. The detailed evolution of the MIBL is important in explaining the behaviour at longer ranges. An extension downwards of the initial region of trapping occurs via the mechanism described in Sec. 5.2. There is also evidence of additional trapping by the growing MIBL, which reaches a height of ~ 300 m towards the end of the range considered. However, there is very little energy still available to be trapped towards the end of the range and therefore the propagation factor remains small between ~ 200 and ~ 300 m. Nonetheless, a radar hole above the MIBL at long ranges can clearly be distinguished.

At midday and during the afternoon, the change from a simple surface duct to an S-shaped duct occurs at a progressively longer range. There tend to be weaker refractivity gradients in the simple surface duct and so trapping is generally a little weaker in the afternoon than in the morning. Variations of the propagation factor within the duct are very sensitive to the development of the S-shape. Consider for example the coverage at 1400 hr. Similarly to the results for the sea–sea path in the high wind case (Sec. 5.2), the propagation factor within the duct has a marked negative vertical gradient. A prominent feature of this diagram is the strong propagation factor between ~ 70 and 200 m at long range. This coincides with the formation and rapid growth of the S-shape (see Fig. 24). Essentially the base of the trapping layer acts as a lid to radar energy in the locally super-refracting environment that constitutes the lowest part of the S-shape. Within that isolated environment, the strong negative gradient of the propagation factor can no longer be maintained and so a more homogeneous vertical distribution arises.

During the evening, the trapping strength diminishes. An example of this can be seen in the coverage diagram at 2000 hr, in which the trapping depth can be seen to increase steadily up to $\sim 200\,\mathrm{m}$. The large values of the propagation factor above the duct indicate that the trapping is not very efficient at this time. Also, the decrease with range of the propagation factor within the duct confirms that it is not difficult for radar energy to escape from the duct.

5.5 Sea–Land Path in Low Winds

We now consider the coverage of a radar transmitter out to sea, which is looking towards the coast. The final 21 km of the path considered pass over land. At the shortest ranges one would expect to find trapping similar to that observed on the sea–sea path described in Sec. 5.1 whereas at longer ranges one expects the duct to decay, resulting in the release of radar energy. These general features can indeed be seen in the coverage diagrams of Fig. 29. From the diagram at 1400 hr on the first day, it is clear that wavelike patterns within the duct occur, as seen along the other paths studied in the low wind case. Escape of energy from the duct appears to be related to the peaks of these waves, leading to a very streaky structure above the duct. This means that although the signal strength overland is in general enhanced by the presence of the duct over the sea, it would not be sensible to rely on such enhancement for the operation of robust communications. During the evening the SBC moves some of the marine air overland, assisting the long–range retention of radar energy at low altitudes. The tendency for overland nocturnal cooling to generate ducting conditions may also contribute to such retention. Thus, the trapping is found to be more persistent at night. Early on the second morning the duct depth increases significantly (see Sec. 5.1) and at sunrise, the nocturnal inversion is quickly burnt off and a strong sea–land contrast re-established. Disintegration of the trapping layer towards the end of the path can be seen as early as 0800 hr. On the second afternoon, the radar energy released from the break-up of the duct is quite large and should allow for good if patchy reception near the coast up to several hundred metres above the surface. It is interesting to note that the trapping layer on the second day seems to retain more of its integrity for somewhat longer than on the first day.

5.6 Sea–Land Path in High Winds

Under high wind conditions the coverage diagrams looking landwards from the sea have a rich structure (Fig. 30). Details of the coverage vary rapidly with time and are highly sensitive to the detailed development of the MIBL. At 1000 hr on the first day, the mature duct height can be seen to be $\sim 300\,\mathrm{m}$ although at short ranges the propagation is strongest below $\sim 200\,\mathrm{m}$. Such

observations are in agreement with the results of Sec. 5.4. The escape of trapped energy begins at a range of $\sim 120\,\text{km}$, which is identical to the location at which trapping first becomes apparent on the land–sea path of Sec. 5.4 at this time. It corresponds to the transition from an S-shaped duct, with the energy largely contained in the lowest part of the S, to a simple surface duct. At midday, there is a region of strong, trapped radar signal throughout the duct at the shorter ranges, and this trapping over the sea is established from the top of the duct downwards as in Sec. 5.2. As the duct height decays energy is released, a process sufficiently fast that the propagation factor just above the surface has been markedly reduced at the coast. There is a yellow streak on the diagram sloping down from $x = 120\,\text{km}$, $z = 240\,\text{m}$ to $x = 160\,\text{km}$, $z = 110\,\text{m}$ which shows that some of the energy in the decaying duct is drawn in to the remaining part of the duct rather than being immediately released. However, this modest resistance to the disintegration of the trapped–energy layer does not delay the inevitable overmuch. Rapid break up of the trapped–energy layer makes the localised radar hole a striking feature of this coverage diagram.

It was stated in Sec. 5.4 that the appearance of an S-shaped duct requires longer fetches as the day progresses. There is also a decrease in the values of ΔM over time. Although modest, these two changes are sufficient to give rise to a different type of propagation behaviour during the afternoon and early evening, a good example being provided by the coverage diagram at 1800 hr. A simple surface duct is present over all of that part of the path that lies over the sea and this supports a somewhat streaky pattern of trapping, below $\sim 210\,\text{m}$ at short ranges. The trapping is initially strongest around the top of the duct but energy becomes concentrated towards the base of the duct as the range increases. This is very similar to the behaviour over the sea–sea path at this time (Sec. 5.2). As the duct decays there is little energy release, presumably because there is little trapped energy in the upper, decaying part of the duct.

By the evening, movement of the SBF inland has transported marine air with an S-shaped duct over the first part of this land–sea path. As a result the coverage diagram at 2200 hr shows elevated trapping at short range. This S-shaped duct is eroded into a two-duct structure with a modest surface duct of about 100 m depth and a weak elevated duct persisting at around 200 m. Thus, there arises a tendency for the trapped energy to become concentrated in two horizontal streaks. While this splitting is occurring, the elevated trapping layer is breaking up, release of energy beginning at a range of $\sim 150\,\text{km}$. The disintegration of the surface duct does not get underway until the coast is reached, at 180 km. Energy release is a much more gradual process at night than in the daytime, essentially because the movement of marine air inland by the SBC produces a smoother transition from ducting to non-ducting conditions.

6 Selection of Refractivity Profiles

The `TERPEM` code allows one to specify a horizontally–varying refractivity environment by means of up to ten vertical profiles (TERPEM User Guide, 1998). Over a propagation range of say 150 km, a typical grid length in the mesoscale model of 6 km implies that 25 profiles are available and thus some of the information from the mesoscale model simulation has to be discarded in defining the refractivity environment within `TERPEM`. An indication that this could have important consequences for the predicted propagation environment is provided by Dockery and Goldhirsh (1995), who estimated that a horizontal resolution of 17 km was necessary in order to obtain 5 dB accuracy in propagation when using a parabolic equation model in a realistic case study with horizontally inhomogeneity. The resolution available in `TERPEM` is close to this estimate.

In situations where meteorological conditions can change rapidly over short horizontal distances the selection of profiles to be used in `TERPEM` may present something of a problem, since the propagation results could vary significantly according to the selection made. The means of selection employed in this report is an automated process designed to restrict the error in specifying the refractivity environment. Sets of profiles within the coverage area are chosen at random, and each such set can be used to define a refractivity environment within `TERPEM` through either step or linear interpolation between the profiles (TERPEM User Guide, 1998). One can estimate an error for each set by selecting mesoscale grid points at random within the coverage area and calculating the RMS difference between the mesoscale model value and the approximate value at that position derived from the specification of the `TERPEM` environment. The set with the lowest error is then used as the actual input to `TERPEM`. As an example of the process consider the high wind run with a 3 km grid length that was described by Plant and Atkinson (2000). Taking a coverage region of $-120 \leq x \leq 50$ km at 1500 hr along the line $y = -54$ km, there are 58 mesoscale grid points available for possible selection. We test 100 profile sets, determining an RMS error for each using 100 randomly–chosen values of M within the coverage region. Since we are mainly interested in the environment within the lowest few hundred metres, we require that these M values be chosen from mesoscale model data for vertical grid points up to 500 m. The variation of the smallest RMS error found with the number of profiles constituting a set is shown in Fig. 31. It should be borne in mind that accuracy above $\sim \pm 1$ M-unit is somewhat superfluous since the semi-empirical formula of Bean *et al.* (1970) is employed in obtaining values of refractivity from the meteorological variables and this is itself subject to errors of $\lesssim 0.5\%$ (Hall, 1979).

From Fig. 31 it is clear that the use by `TERPEM` of linear interpolation in the horizontal is desirable when transferring data from the mesoscale model. The coverage region considered is a heterogeneous one, incorporating the

growth of a marine internal boundary layer (Plant and Atkinson, 2000) in a transition from land to sea conditions. Encouragingly, even for such a coverage region, Fig. 31 suggests that the ten profiles permitted by TERPEM should be sufficient to provide an accurate description of the refractivity environment predicted by the mesoscale model. The distribution of RMS errors from 100 sets of ten profiles is shown in the lower plot of Fig. 31. The median random selection has an error of $\sim 2.4\,M$-units. In general, one would expect that a uniform spacing of the profiles or the choice of a skilled user would produce a rather smaller error than a typical random selection. According to the figure, the error would be reduced to 1.5–2.0 M-units by a user who was able to beat 65–85% of the random selections.

From Sec. 5.4, the coverage expected along the land–sea path at this time has fairly weak trapping at low altitudes, the trapping layer deepening gradually with increasing range. Although a different high wind run is considered here and the time is a little later, the diagram should be broadly similar to the lower left plot of Fig. 28. This is indeed the case when using the optimally–selected set of refractivity profiles, as can be seen from Fig. 32. This set had an RMS error of 0.8 M-units. In Fig. 33 we show the TERPEM results obtained using two other sets of profiles, one having an error of 1.5 M-units, which seems reasonable for a skilled user, and the other having an error of 2.4 M-units, corresponding to the median random selection. The coverage diagrams of Fig. 33 have an altogether different character. They exhibit elevated trapping at the longer ranges between ~ 200 and 300 m, in agreement with Fig. 32, but predict a radar hole rather than a region of weak trapping at low altitudes. These results demonstrate that quite subtle changes to the specified refractivity environment can have a significant effect on the predicted coverage. Moreover, it is clear that the detailed method of transferring data from the mesoscale model to TERPEM deserves some attention.

As a further illustration of the effects of such errors, the reader should compare Fig. 9 with the upper plot of Fig. 11. These two coverage diagrams refer to the same situation, the configuration differing only in the set of refractivity profiles that was used in the TERPEM run. Each set of profiles was derived a separate application of the automated selection process described above and both sets had an RMS error $\leq 1\,M$-unit. Although there is good, broad agreement between the two coverage diagrams there are also some noticeable differences in the details.

7   Discussion and Conclusions

Previous reports from this project have described the use of a mesoscale meteorological model for prediction of the refractivity environment over the Persian Gulf (Li and Atkinson, 1998b; Plant and Atkinson, 1999, 2000). In

this report we have used results from such mesoscale model runs as input to the code `TERPEM`, which can be used to predict the propagation environment (TERPEM User Guide, 1998). In Sec. 3 we performed some checks on the operation of this code. Some general points about radar propagation within the modelled ducts were presented in Sec. 4, being highlighted through comparison with the modelling of Brooks *et al.* (1999) and through examination of the effects of varying transmitter or other `TERPEM` parameters. Radar propagation over the Gulf under the complex, horizontally–varying refractivity conditions predicted by the mesoscale model was studied in Sec. 5. Details of the coupling between the mesoscale model and `TERPEM` have also been considered, not least the mechanisms for interpolation of refractivity data in both the horizontal and the vertical.

7.1   The Propagation Environment

The mesoscale model runs of Li and Atkinson (1998b) and Plant and Atkinson (1999, 2000) aimed to simulate the refractivity environment in the period of aircraft observations reported by Brooks *et al.* (1997, 1999). The observations were divided by Brooks *et al.* (1997, 1999) into low and high wind cases, characterised by typical wind speeds of $5\,\mathrm{ms}^{-1}$ and $15\,\mathrm{ms}^{-1}$ respectively in the predominant air flow from Saudi Arabia over the Gulf waters. The same distinction has been made in the modelling. Since the ducting conditions vary significantly between the two cases, they have also been considered separately within this report.

In the low wind case, a simple surface duct of about $100\,\mathrm{m}$ is present over the Gulf during the afternoon of the first day. The refractivity difference across the duct is large ($\sim 80\,M$-units), resulting in strong trapping over the full extent of the duct. By contrast, the duct in the high wind case is about three times as deep, but with a refractivity difference about half as large, which results in less powerful trapping. Within $\sim 100\,\mathrm{km}$ or so from the coast a simple surface duct also occurs in the high wind case, but further out to sea an S-shaped duct develops, the base of the trapping layer lying about $200\,\mathrm{m}$ above the sea surface. This development can have a significant impact on propagation, particularly if the coverage region includes a transition between the two types of duct. For example, trapping of radar energy sent from land to sea through the evolving duct becomes notably more efficient once the S-shaped duct is established. The presence of the S-shaped duct in the high wind case means that the propagation factor within the duct tends to exhibit more variation in the vertical in this case.

During the late afternoon and early evening, a sea–breeze circulation becomes established and the downwind subsidence in the circulation reduces the duct height. Movement of marine air coastwards by the SBC smooths out the horizontal gradients between the land and sea air masses and has important effects on the propagation around the coast. Signals sent from

land to sea at this time are more easily captured by the growing duct whilst signals sent from sea to land escape less readily from the decaying duct. Mesoscale model runs for the high wind case break down during the early hours of the morning (Li and Atkinson, 1998b). In the low wind case, however, the duct is seen to deepen during the early hours, reaching $\sim 150\,\mathrm{m}$ and retaining this height through to the afternoon of the second day. The inversion at the top of the MIBL is tighter on the second day than the first, leading to stronger trapping.

The propagation factor within the duct exhibits an interesting horizontal wavelike pattern in the low wind case. Such waves can occur within a homogeneous refractivity environment. Escape of energy from the duct has sometimes been seen to be favourable at the peaks, particularly at the longer ranges. At short ranges, the positions of the first peaks have been correlated with the nulls in the interference pattern of sea–surface reflections, at least for high radar frequencies.

7.2 Some Comments on `TERPEM`

The authors of this report have found the `TERPEM` package straightforward to use. Happily, the execution times required by the code were short and did not pose any difficulties, being no more than a minute or so in all instances. However, one small issue concerns the input of meteorological data, the TERPEM User Guide (1998) recommending that this be entered by loading a file of height–refractivity pairs for each vertical profile required. Loading ten separate files for each `TERPEM` run can become a little tedious and mistakes by the user in following this procedure seem possible, particularly if there are a large number of `TERPEM` runs to be set up. Moreover, it is suggested below that the number of horizontal positions at which a profile can be specified might profitably be increased in the code. If many profiles were to be input, it would become desirable to adopt an easier method for entering the large amounts of data. The present authors have found it convenient to use a short piece of postprocessing code in order to turn output from the mesoscale model into `*.met` files suitable for immediate use with `TERPEM`. If the authors of a future User Guide were to supply information about the precise format of the `*.met` input file then other users would be able to write similar code for themselves very quickly.

The modelling capabilities of the `TERPEM` code could be usefully enhanced by allowing for variations in the wind speed parameter that is used in making roughness calculations (see Sec. 4.2), by reviewing the method of roughness calculation over land and by increasing the number of horizontal positions at which data can be specified. This final point would allow for exploitation of all the information available in the mesoscale model predictions. The limit of ten horizontal positions inevitably causes the strong horizontal gradients between land and sea air (Plant and Atkinson, 1999) to be smoothed out

in the refractivity environment suppiled to the `TERPEM` code. Given the statement by Dockery (1988, page 1468) about the numerical method that:

> Aside from slight differences due to the extra interpolations required between profiles, the complexity of the environment has no impact on the time required for calculation.

the limit imposed in the current version of `TERPEM` does appear to be unduly and artificially restrictive. It may be reasonable if the meteorological data is derived from a limited density of observations or is merely idealized, but is not appropriate for data derived from a high–resolution mesoscale model.

7.3   Implications for Practical Prediction

The analysis using `TERPEM` of refractivity environments predicted by the mesoscale model has been generally encouraging. Although it is clear that small changes to the refractivity environment (well within the range of probable errors in the predicted field) can produce large and important changes in the predicted propagation environment, the power of the mesoscale model has also been apparent. The refractivity field provided by the model is sufficiently detailed that some quite subtle influences on the propagation environment can be distinguished. Also, it should be borne in mind that errors in observations of the refractivity field can themselves be important[6] and that there are considerable uncertainties associated with forced assumptions of spatial and temporal homogeneity. The use of a mesoscale model allows one the valuable opportunity to investigate the propagation at arbitrary times and places. The ability to study realistic situations for which little or no observational data is available may lead to an improved qualitative understanding of propagation characteristics under complex ducting conditions. For example, studies like those of Sec. 5 may help to elucidate the patterns of growth or decay of ducts over ranges of several tens of kilometres from the coast. For purely practical prediction, mesoscale models offer a tool for making sensible interpolations between routine observation profiles, which tend to be widely–spaced and infrequent.

---

[6]Brooks *et al.* (1999, Table 1) quote an error of 1% for ship–based measurements of relative humidity. An error of similar size would hold for the derived refractivity. Evidence that such an error could have an important impact on the predicted propagation environment is given in Sec. 6.

References

Abdul-Jauwad, S. H., Khan, P. Z. and Halawani, T. O. 1991. Prediction of Radar Coverage under Anomalous Propagation Conditions for a Typical Coastal Site: A Case Study. *Radio Sci.*, **26**, 909–919.

Barrios, A. E. 1989. Terrain and Refractivity Effects on Non-Optical Paths. *In: Multiple Mechanism Propagation Paths (MMPPs): Their Characterisation and Influence on System Design*. AGARD Conference Proceedings, vol. 543. Paper 10.

Battan, L. J. 1973. *Radar Observation of the Atmosphere*. University of Chicago Press. 324pp.

Baumgartner Jr, G. B. 1983. *XWVG: A Waveguide Program for Trilinear Tropospheric Ducts*. Tech. Rept. 610. Naval Ocean Systems Center, San Diego.

Bean, B. R., Dutton, E. J. and Warner, B. D. 1970. Weather Effects on Radar. *Chap. 24 of:* Skolink, M. I. (ed), *Radar Handbook*, 2nd edn. McGraw–Hill Book Company.

Bogush Jr, A. J. 1989. *Radar and the Atmosphere*. Artech House. 452pp.

Brooks, I. M., Rogers, D. P. and Goroch, A. K. 1997. *SHAREM-115 Observations: Atmospheric Environmental Data Collected by the UK Meteorological Research Flight C-130 Hercules Aircraft*. unpublished report available from ftp://megan.ucsd.edu/pub/sharem, 53pp.

Brooks, I. M., Goroch, A. K. and Rogers, D. P. 1999. Observations of Strong Surface Radar Ducts over the Persian Gulf. *J. Appl. Meterol.*, **38**, 1293–1310.

Budden, K. G. 1961. *The Wave–Guide Theory of Wave Propagation*. Logos Press, Prentice Hall Inc. 325pp.

Cole, H. W. 1985. *Understanding Radar*. William Collins Sons & Co. Ltd. 267pp.

Collin, R. E. 1985. *Antennas and Radiowave Propagation*. McGraw–Hill Book Company. 508pp.

Craig, K. H. 1988. Propagation Modelling in the Troposphere: Parabolic Equation Method. *Elec. Lett.*, **24**, 1136–1139.

Dockery, G. D. 1988. Modelling Electromagnetic Wave Propagation in the Troposphere Using the Parabolic Equation. *IEEE Trans. Antenn. Prop.*, **36**, 1464–1470.

Dockery, G. D. and Goldhirsh, J. 1995. Atmospheric Data Resolution Requirements for Propagation Assessment: Case Studies of Range–Dependent Coastal Environments. *In: Propagation Assessment in Coastal Environment*. AGARD Conference Proceedings, vol. 567. Paper 7.

Felsen, L. B. 1981. Hybrid Ray–Mode Fields in Inhomogeneous Waveguides and Ducts. *J. Acoust. Soc. Am.*, **69**, 352–361.

Goldhirsh, J. and Dockery, D. 1998. Propagation Factor Errors Due to the Assumption of Lateral Homogeneity. *Radio Sci.*, **33**, 239–249.

Gossard, E. E. 1983. *Radar Observations of Clear Air and Clouds*. Elsevier Science Publishers. 280pp.

Hall, M. P. M. 1979. *Effects of the Troposphere on Radio Communication*. Institute of Electrical Engineers. 206pp.

Joseph, R. I. and Smith, G. D. 1972. Propagation in an Evaporation Duct: Results in Some Simple Analytic Models. *Radio Sci.*, **7**, 433–441.

Kerr, D. E. 1951. *Propagation of Short Radio Waves*. McGraw Hill, New York.

Kukushkin, A. V. and Sinitsin, V. G. 1983. Rays and Modes in a Nonuniform Troposphere. *Radio Sci.*, **18**, 573–581.

Levy, M. F. 1989. Combined Effects of Atmosphere and Terrain on UHF/Microwave Paths. *In: Multiple Mechanism Propagation Paths (MMPPs): Their Characterisation and Influence on System Design.* AGARD Conference Proceedings, vol. 543. Paper 10.

Levy, M. F. 1995. Fast PE Models for Mixed Environments. *In: Propagation Assessment in Coastal Environment*. AGARD Conference Proceedings, vol. 567. Paper 8.

Li, J.-G. and Atkinson, B. W. 1997a. *Numerical Modelling of the Propagation Environment in the Atmospheric Boundary Layer Over Coastal Areas: Literature Review and Mesoscale Model*. Tech. Rept. 1. MoD Agreement NNR/2042/1. 36pp.

Li, J.-G. and Atkinson, B. W. 1997b. *Numerical Modelling of the Propagation Environment in the Atmospheric Boundary Layer Over Coastal Areas: Model Sensitivity Study*. Tech. Rept. 2. MoD Agreement NNR/2042/1. 69pp.

Li, J.-G. and Atkinson, B. W. 1998a. *Numerical Modelling of the Propagation Environment in the Atmospheric Boundary Layer Over Coastal Areas: Idealised Case Study*. Tech. Rept. 3. MoD Agreement NNR/2042/1. 65pp.

Li, J.-G. and Atkinson, B. W. 1998b. *Numerical Modelling of the Propagation Environment in the Atmospheric Boundary Layer Over Coastal Areas: Real Case Study — The Persian Gulf.* Tech. Rept. 4. MoD Agreement NNR/2042/1. 42pp.

Lystad, S. and Tjelta, T. 1995. High Resolution Meteorological Grid for Clear Air Propagation Modelling in Northern Coastal Regions. *In: Propagation Assessment in Coastal Environment.* AGARD Conference Proceedings, vol. 567. Paper 41.

Miller, A. R., Brown, R. M. and Vegh, E. 1984. New Derivation for the Rough–Surface Reflection Coefficient and for the Distribution of Sea–Wave Elevations. *IEE Proc. Part H*, **131**, **2**, 114–116.

Paulus, R. A. 1989. The Lorentz Reciprocity Theorem as a Consistency Test for Propagation Models. *In: Multiple Mechanism Propagation Paths (MMPPs): Their Characterisation and Influence on System Design.* AGARD Conference Proceedings, vol. 543. Paper 17.

Phillips, O. M. 1966. *Dynamics of the Upper Ocean.* Cambridge University Press.

Plant, R. S. and Atkinson, B. W. 1999. *Numerical Modelling of the Propagation Environment in the Atmospheric Boundary Layer of Littoral Areas — Resolution Effects.* Tech. Rept. 1. MoD Agreement FS2/2042/02. 61pp.

Plant, R. S. and Atkinson, B. W. 2000. *Numerical Modelling of the Propagation Environment in the Atmospheric Boundary Layer of Littoral Areas — Horizontal Variations in the Marine Boundary Layer.* Tech. Rept. 2. MoD Agreement FS2/2042/02. 69pp.

Rogers, L. T. 1995. Effects of Spatial and Temporal Variability of Atmospheric Refractivity on the Accuracy of Propagation Assessments. *In: Propagation Assessment in Coastal Environment.* AGARD Conference Proceedings, vol. 567. Paper 31.

Skolink, M. I. 1980. *Introduction to Radar Systems.* McGraw Hill Book Company. 581pp.

TERPEM User Guide. 1998 (June). *TERPEM User Guide.* Signal Science Limited, 20, Alexander Close, Abingdon, Oxon. OX14 1XA. UK. Code version 5.1.

Turton, J. D., Bennetts, D. A. and Farmer, S. F. G. 1988. An Introduction to Radio Ducting. *Meteorol. Mag.*, **117**, 245–254.

Wait, J. R. 1980. Coupled Mode Analysis for a Nonuniform Wave Guide. *Radio Sci.*, **15**, 667–673.
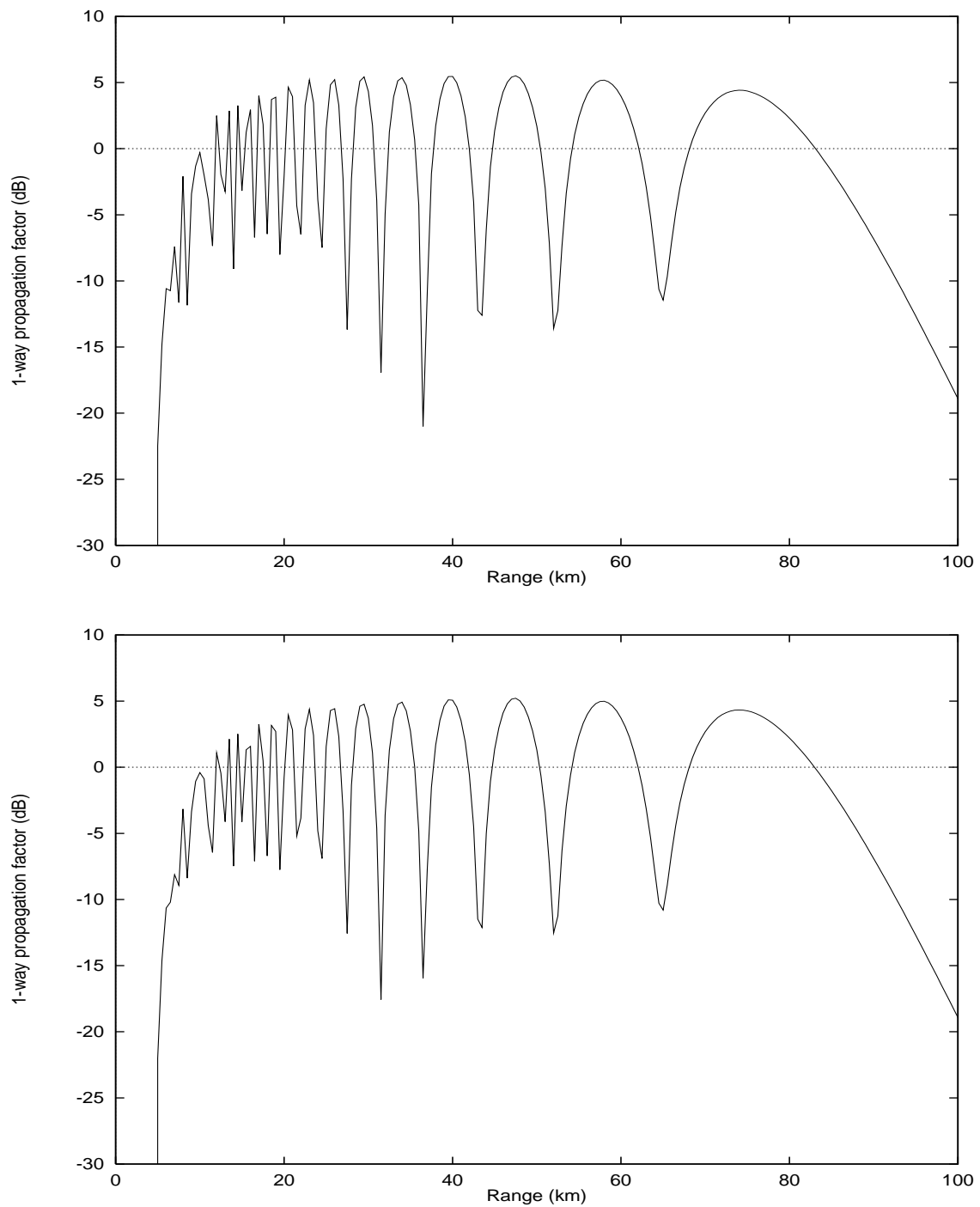
Figure 1: The 1-way propagation factor (dB) as a function of range (km) from two tests of the TERPEM code (Sec. 3). Horizontal and vertical polarizations are used in the upper and lower plots respectively. These plots should be compared to Figs. 2 and 3 of Dockery (1988).

33
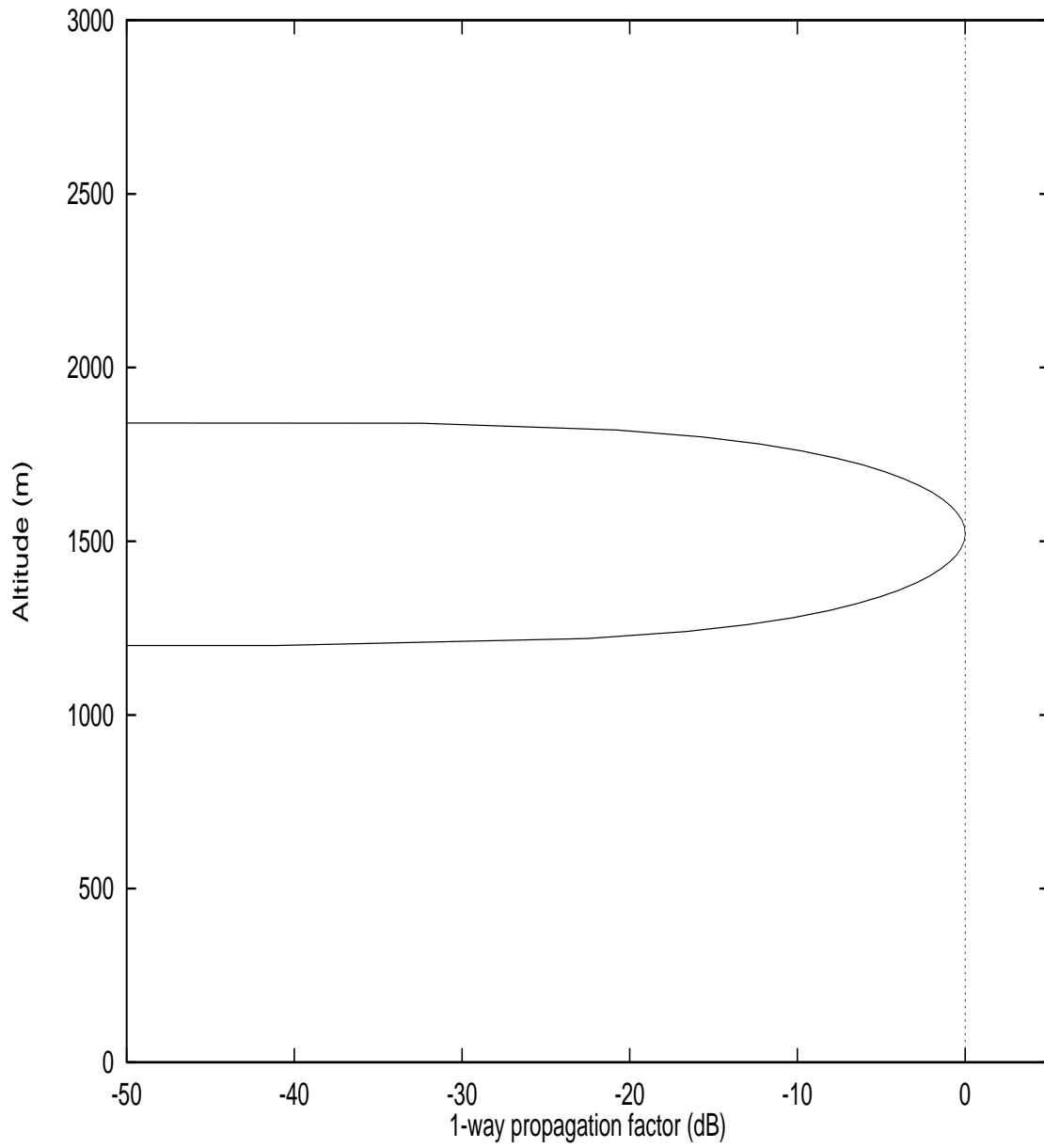
Figure 2: The 1-way propagation factor (dB) as a function of altitude (m) from the third test of the TERPEM code (Sec. 3). The plot should be compared to Fig. 4 of Dockery (1988).
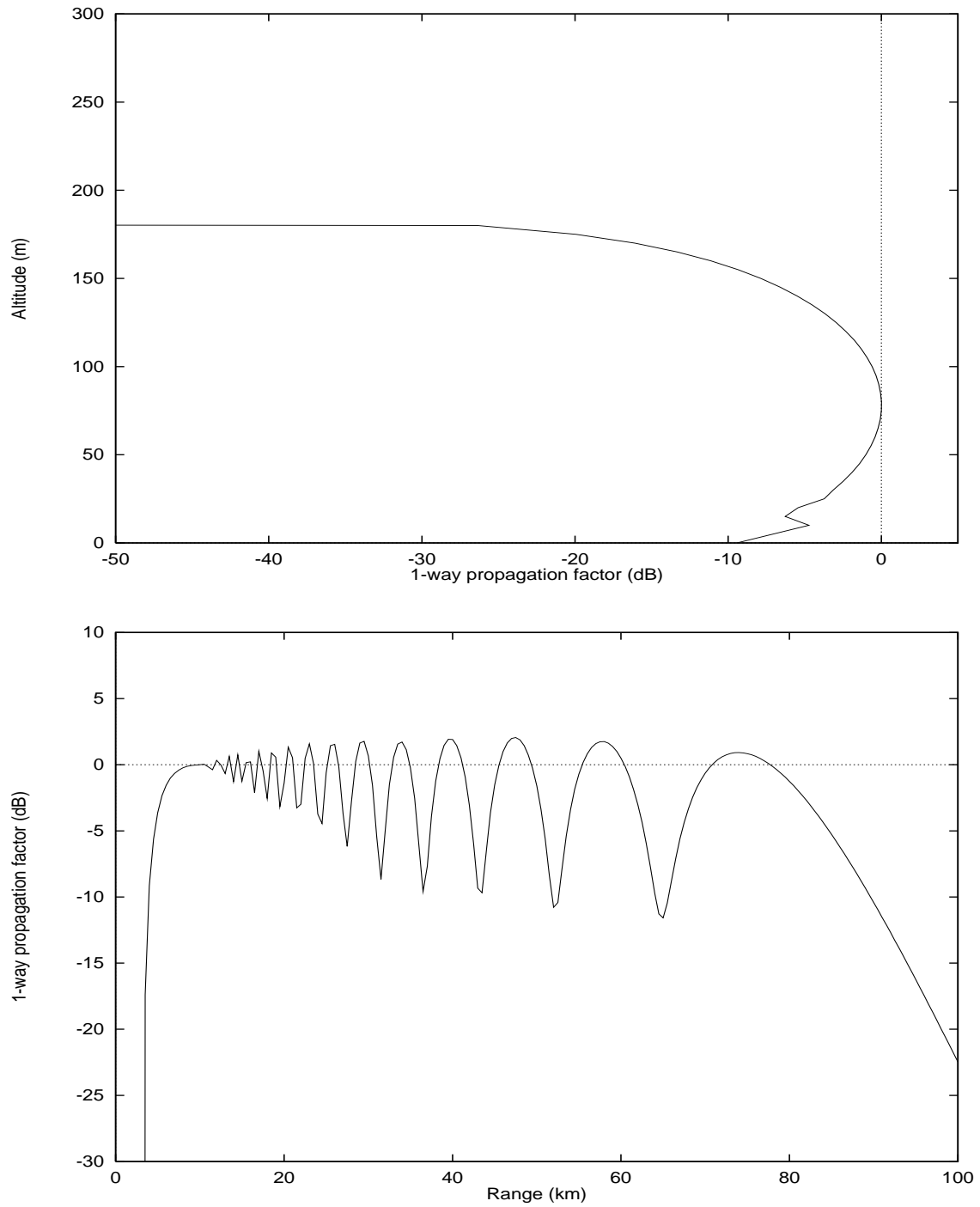
Figure 3: Results from the fourth and fifth tests of the TERPEM code (Sec. 3). The upper plot shows the 1-way propagation factor (dB) as a function of altitude at short range; the lower plot shows this factor as a function of range (km) at an altitude of 305 m. These plots should be compared to Figs. 5 and 6 of Dockery (1988).

35
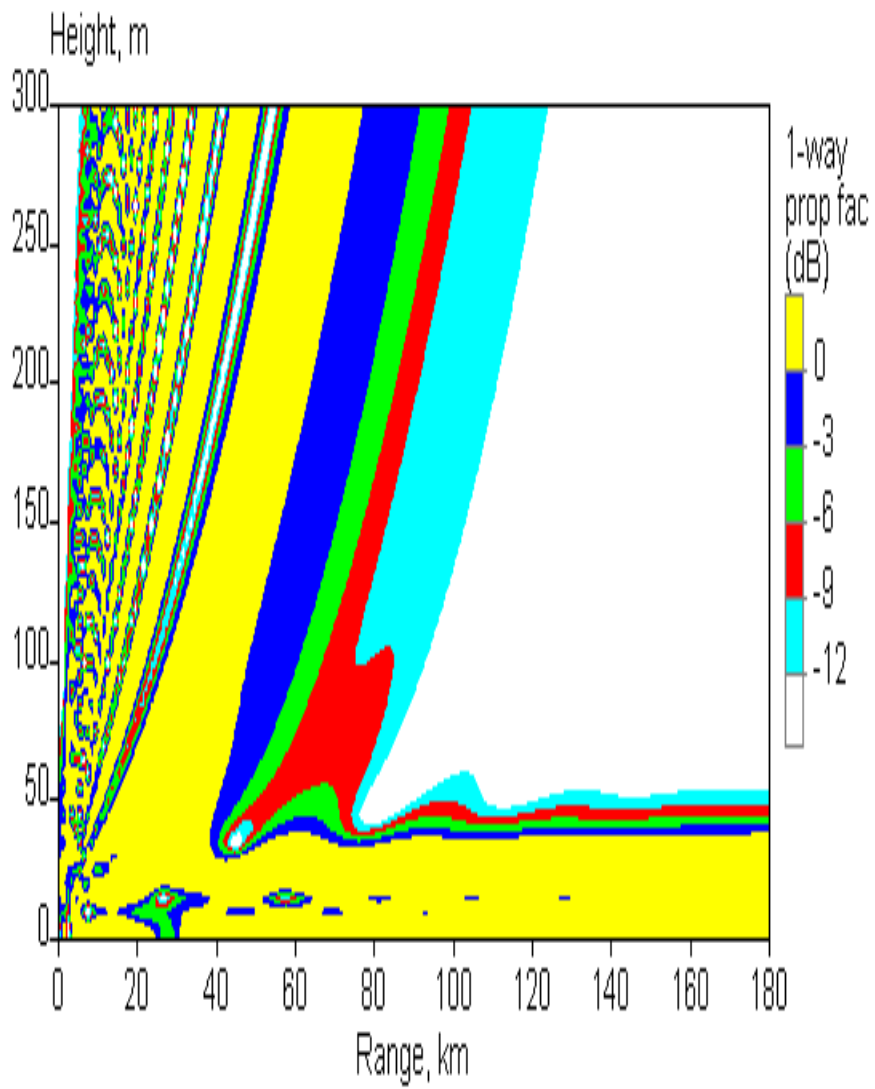
Figure 4: A coverage diagram showing the 1-way propagation factor (dB) from a uniform–duct test of the TERPEM code (Sec. 3). The plot should be compared to Fig. 7 of Dockery (1988).

36
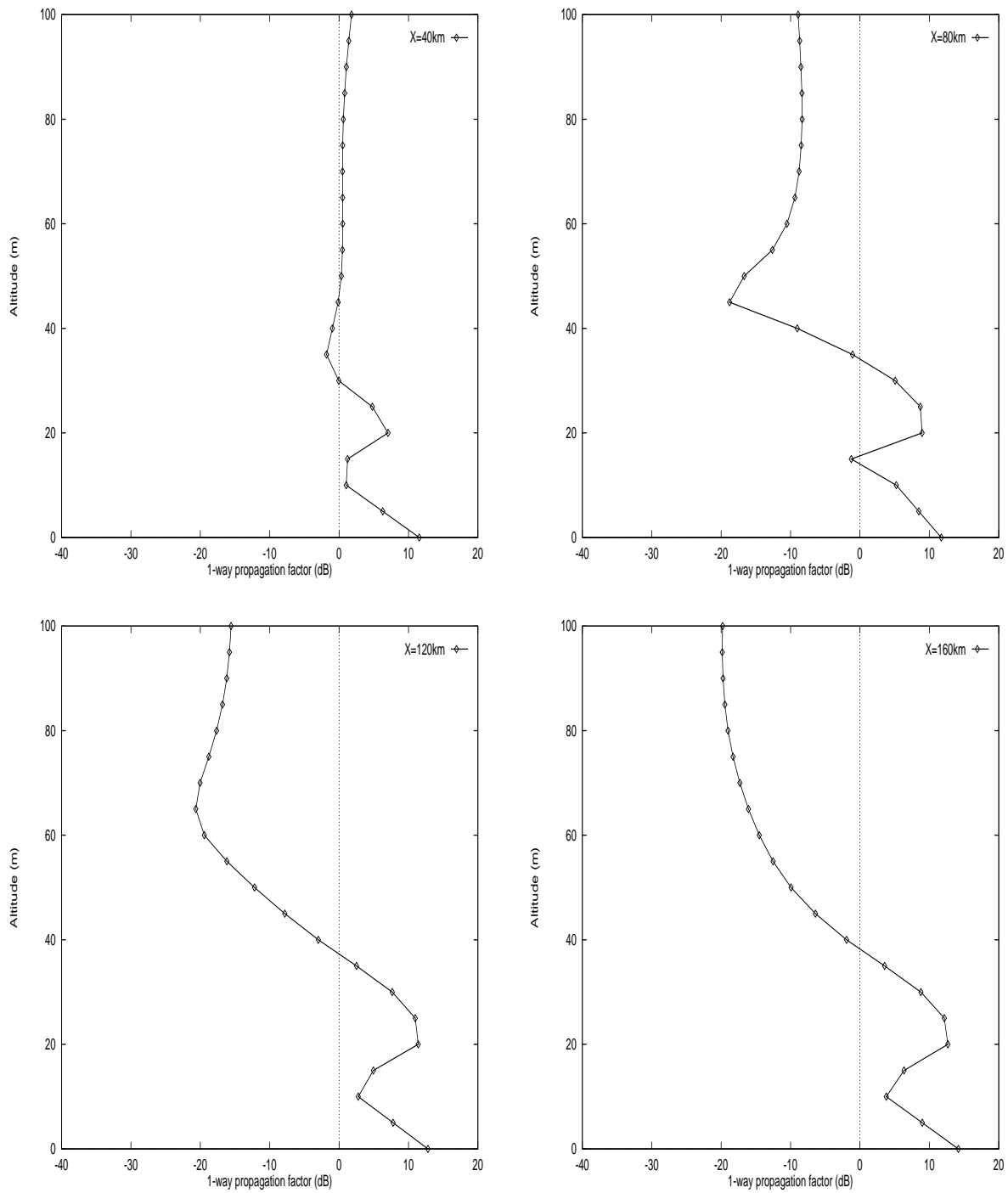
Figure 5: The 1-way propagation factor (dB) is plotted as a function of altitude (m) for several ranges from a uniform–duct test of the `TERPEM` code (Sec. 3). The plot should be compared to Fig. 8 of Dockery (1988).

37
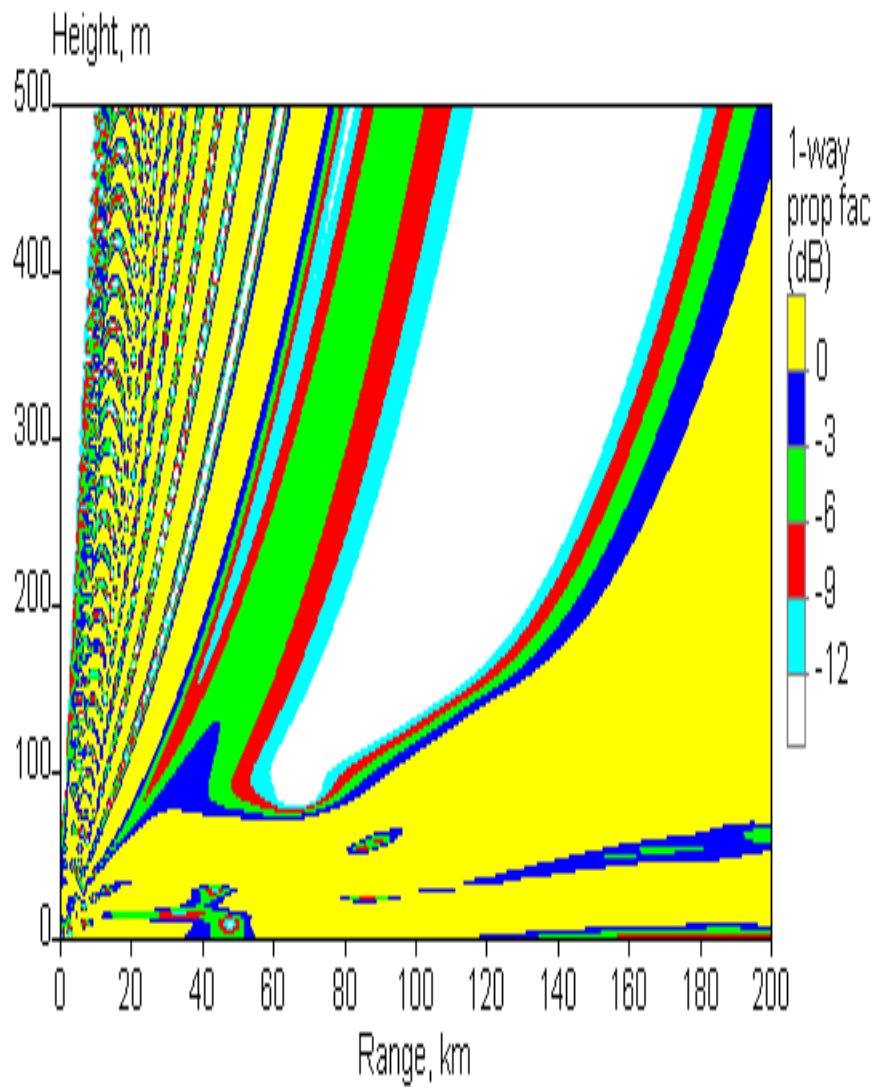
Figure 6: A coverage diagram showing the 1-way propagation factor (dB) from an inhomogeneous–duct test of the TERPEM code (Sec. 3). The plot should be compared to Fig. 9 of Dockery (1988).
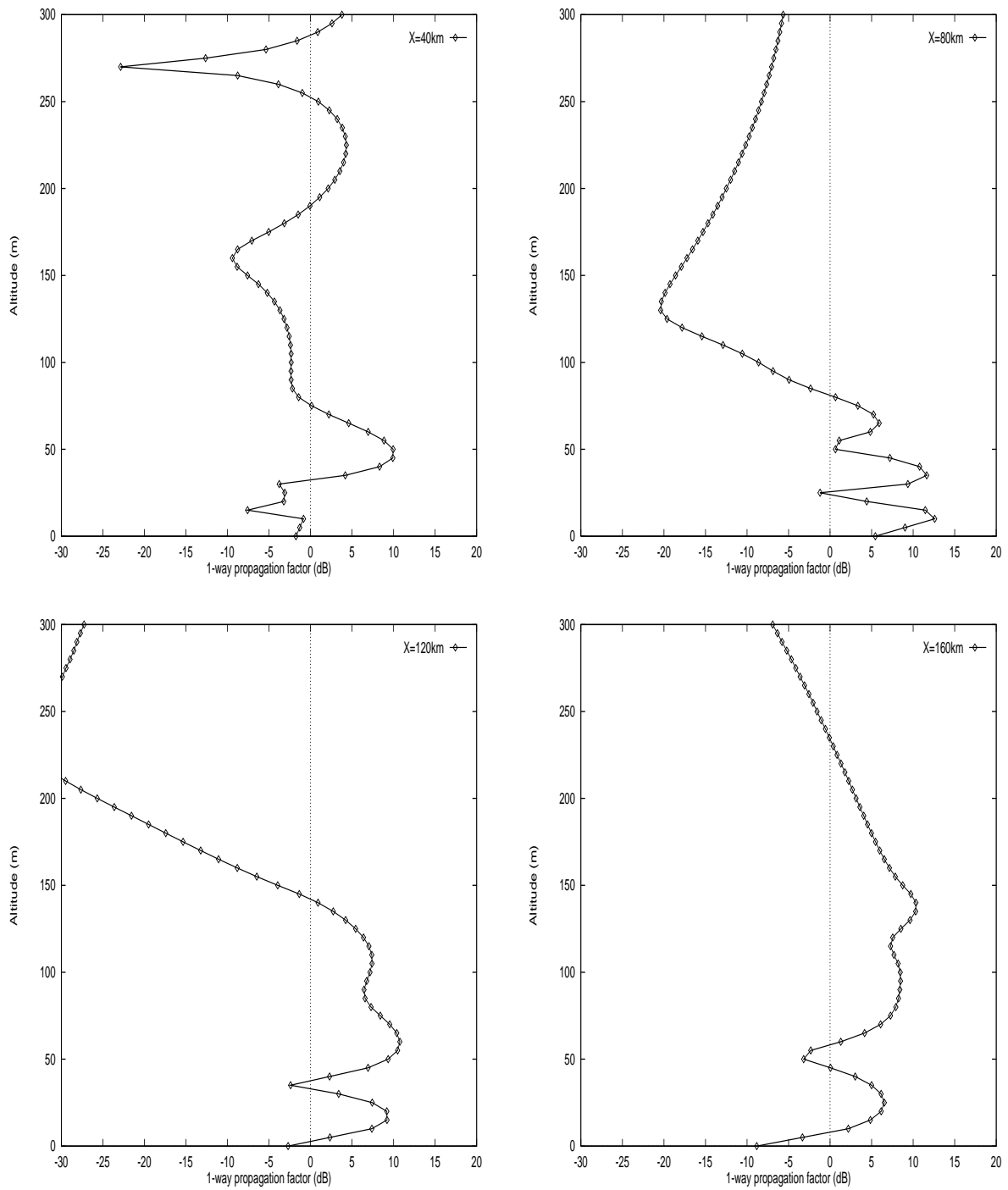
Figure 7: The 1-way propagation factor (dB) is plotted as a function of altitude (m) for several ranges from an inhomogeneous–duct test of the TERPEM code (Sec. 3). The plot should be compared to Fig. 10 of Dockery (1988).
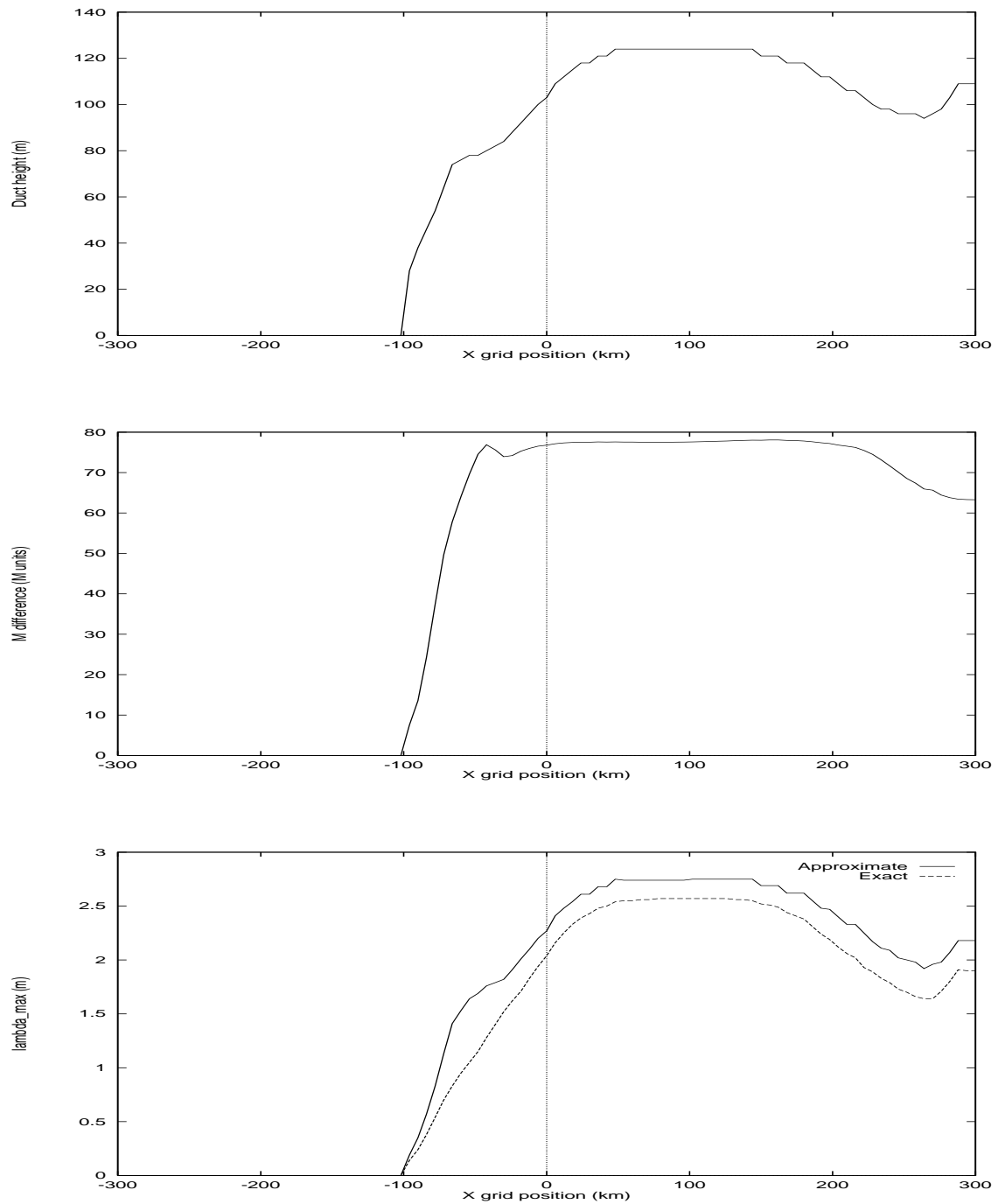
Figure 8: Duct parameters along the line $y = -54\,\text{km}$ at $1400\,\text{hr}$ on the first day of a low wind run (Plant and Atkinson, 1999). The upper plot shows the duct height (m), the middle plot shows the modified refractivity difference across the duct (M-units) and the lower plot shows the maximum wavelength (m) of radiation that can be trapped by the duct. The lower plot shows the results from an exact calculation (Eq. 3) and from an approximate formula (Eq. 4).
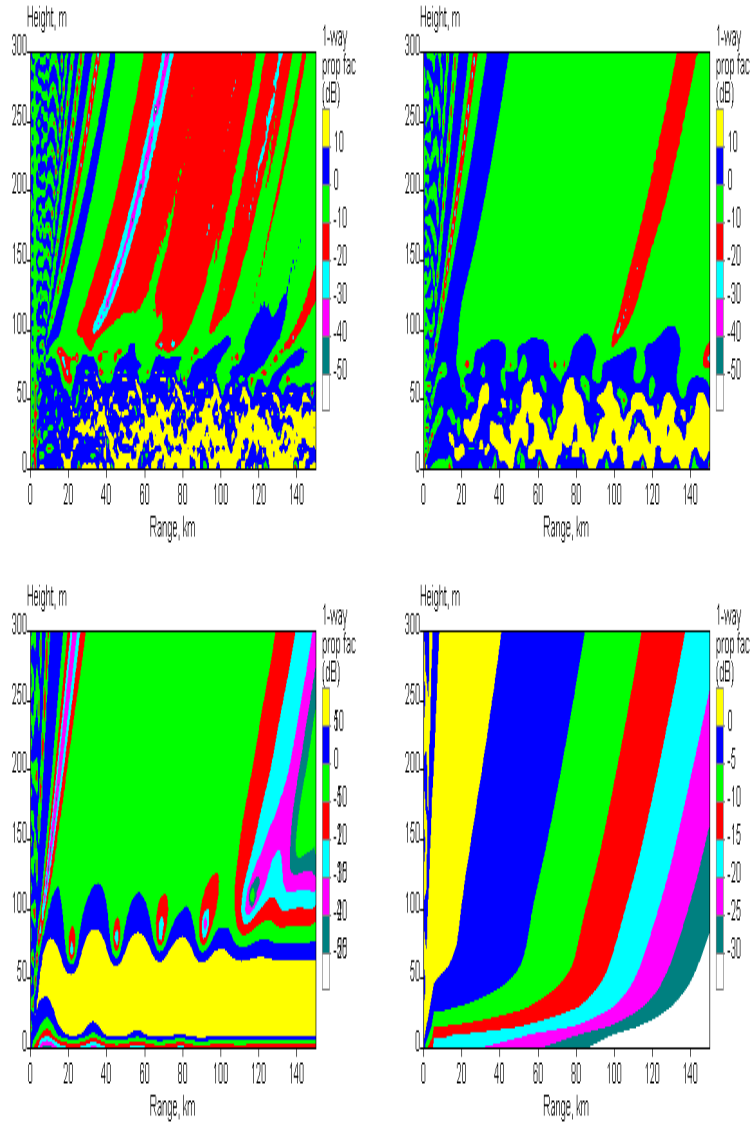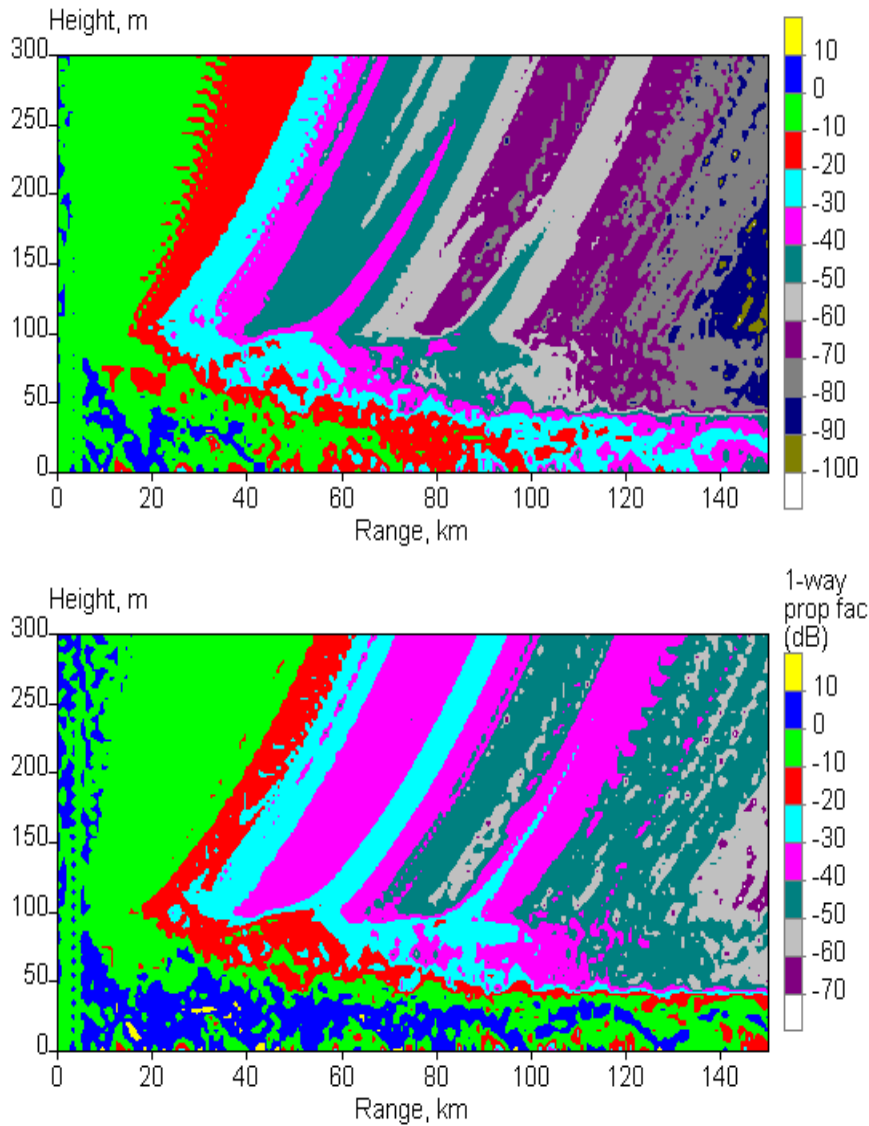
40
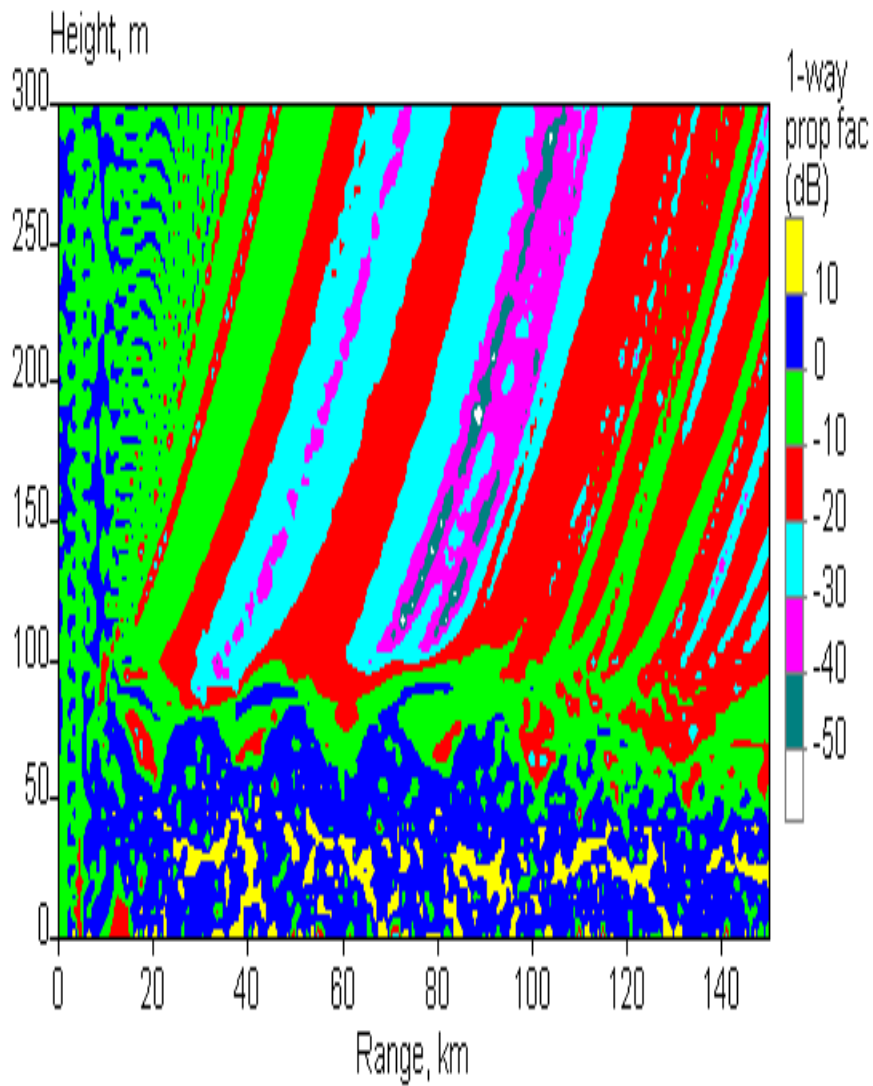
Figure 9: A coverage diagram showing the 1-way propagation factor (dB) along the line $y = -54\,\mathrm{km}$ at 1400 hr on the first day of a low wind run (Plant and Atkinson, 1999). A 10 GHz circularly–polarized radar was positioned 30 m above the surface at $x = 120\,\mathrm{km}$.
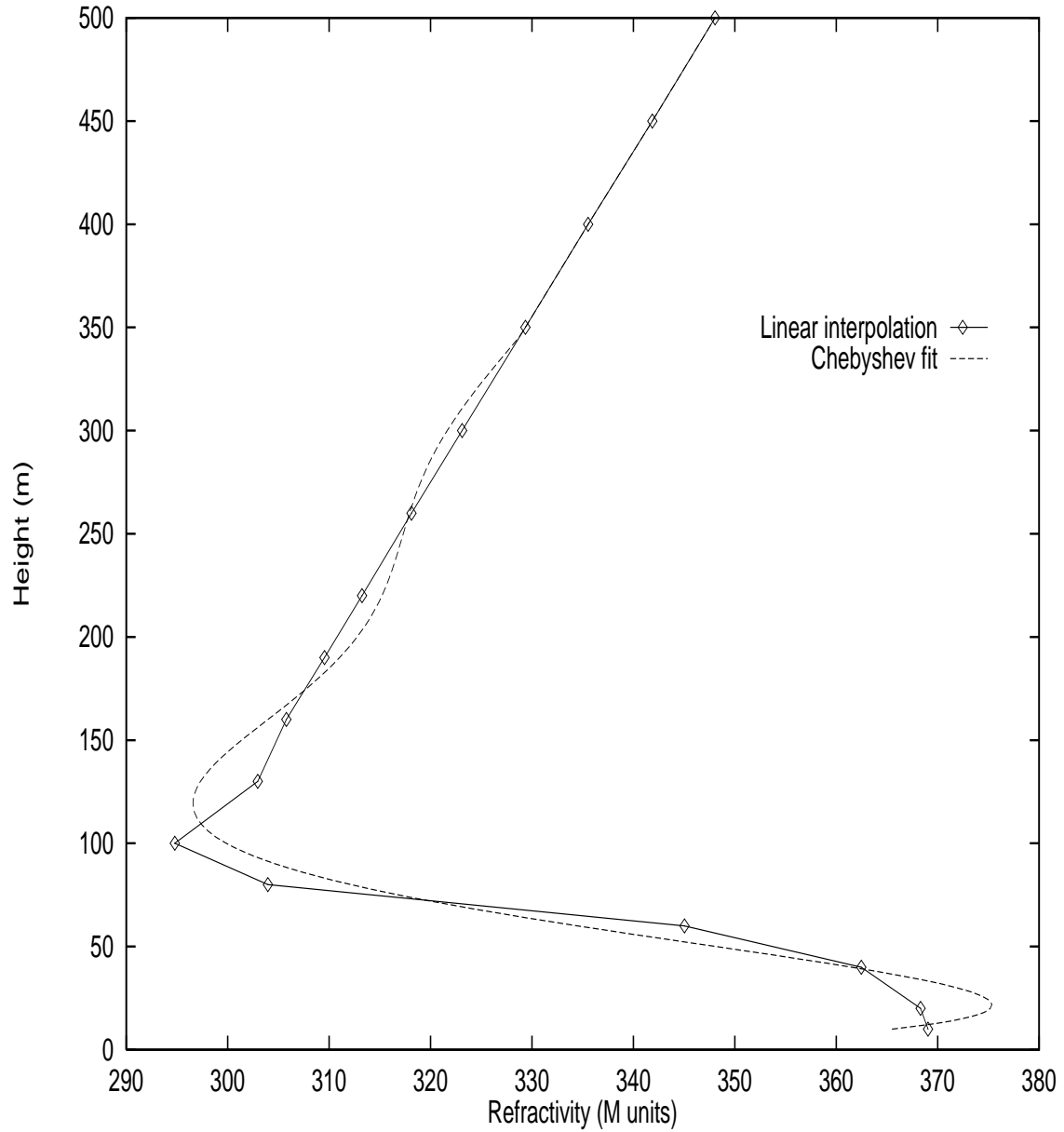
Figure 10: The modified refractivity profile at $x = 132\,\mathrm{km}$ and $y = -54\,\mathrm{km}$ for 1400 hr on the first day of a low wind run (Plant and Atkinson, 1999). Linear interpolation is made between the vertical grid point values. Also shown is a Chebyshev fit (Plant and Atkinson, 2000) to this profile.
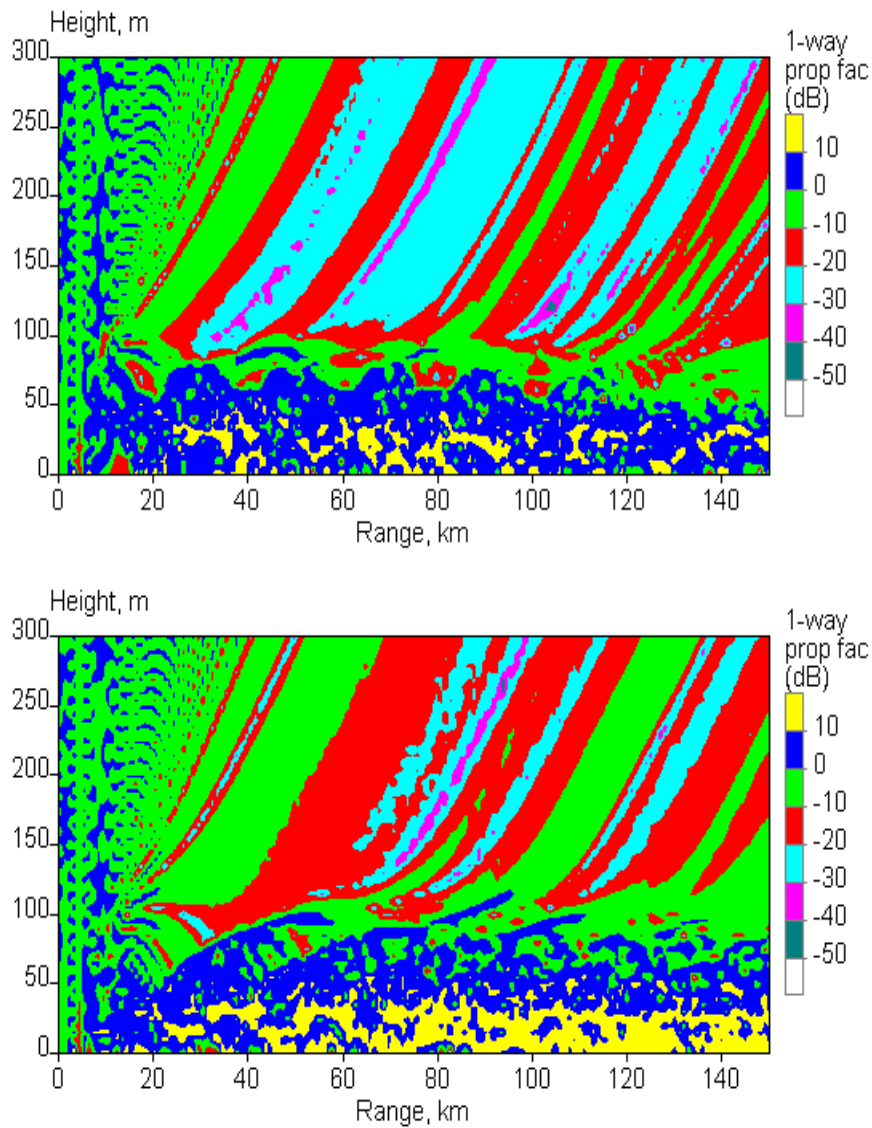
Figure 11: Coverage diagrams showing the 1-way propagation factor (dB) along the line $y = -54$ km at 1400 hr on the first day of a low wind run (Plant and Atkinson, 1999). A 10 GHz circularly–polarized radar was positioned 30 m above the surface at $x = 120$ km. In the upper diagram, the input data to TERPEM consisted of values at the mesoscale grid heights only. In the lower diagram, the input data was interpolated to intermediate heights using a fit to the mesoscale grid values.

43
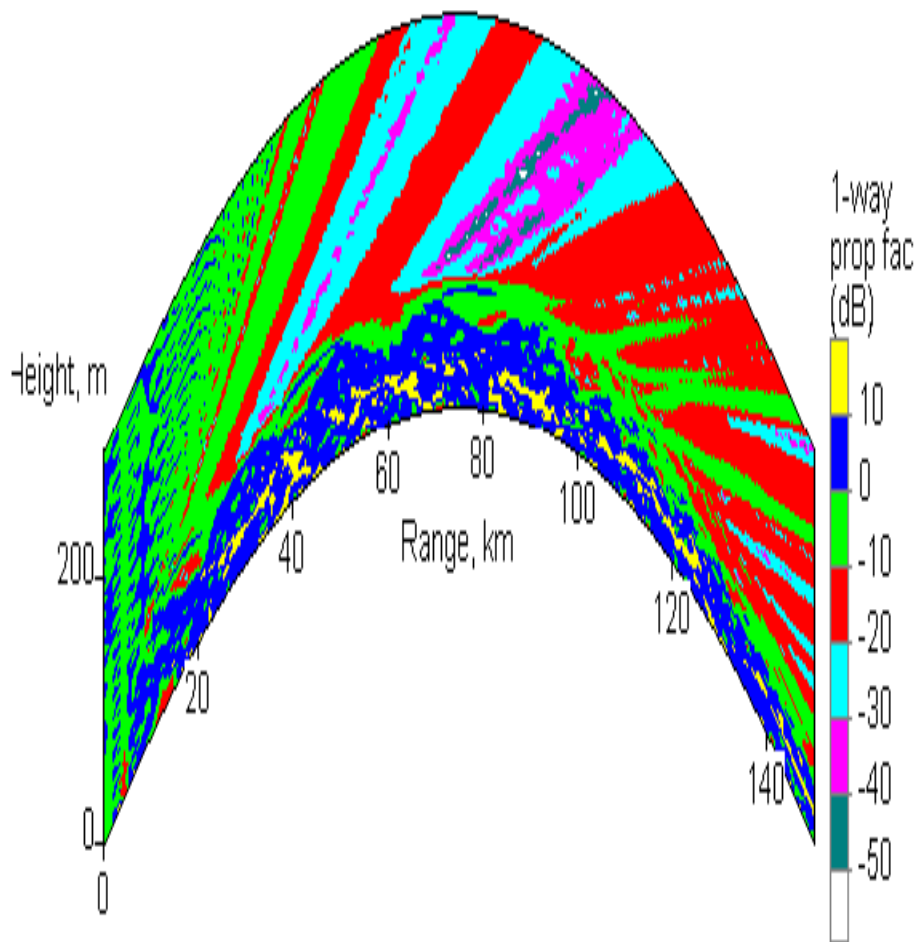
Figure 12: A flat–earth coverage diagram showing the 1-way propagation factor (dB) along the line $y = -54\,$km at 1400 hr on the first day of a low wind run (Plant and Atkinson, 1999). A 10 GHz circularly–polarized radar was positioned 30 m above the surface at $x = 120\,$km.
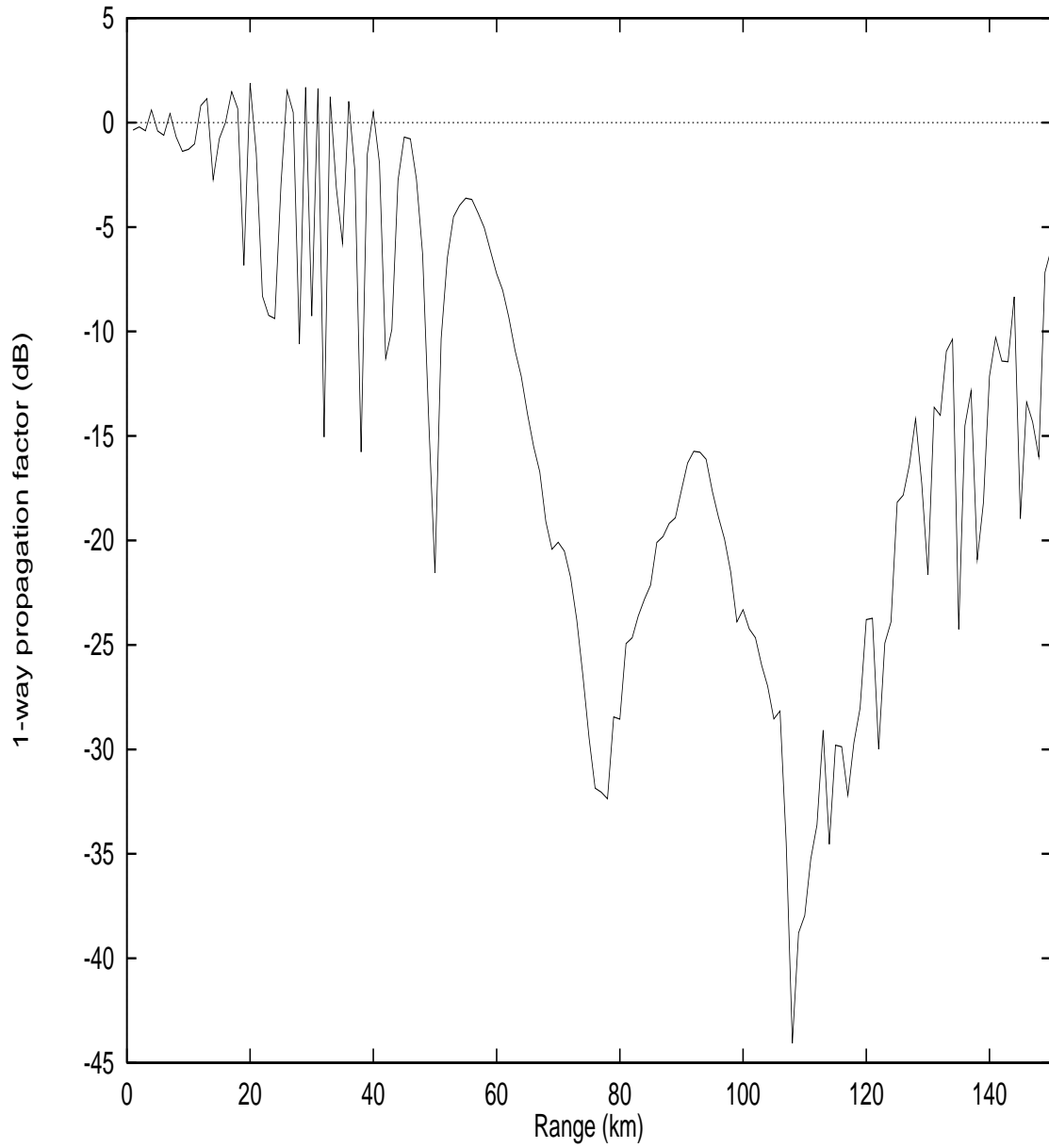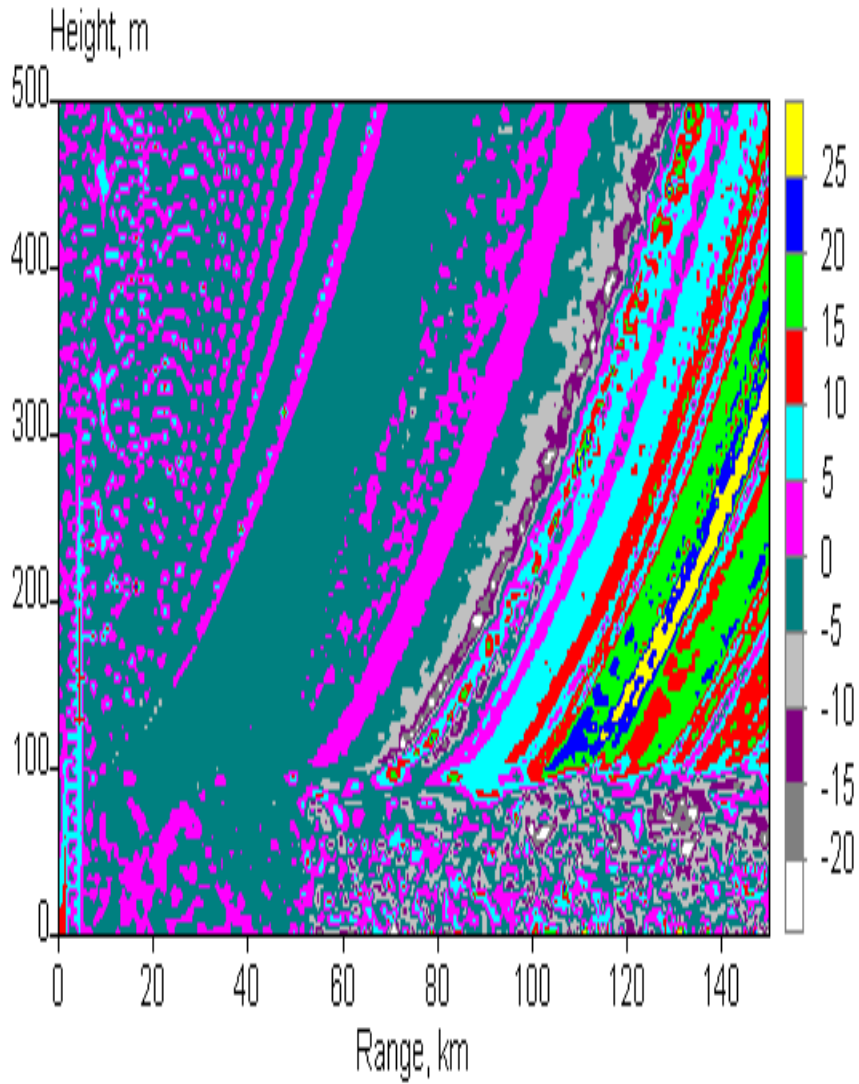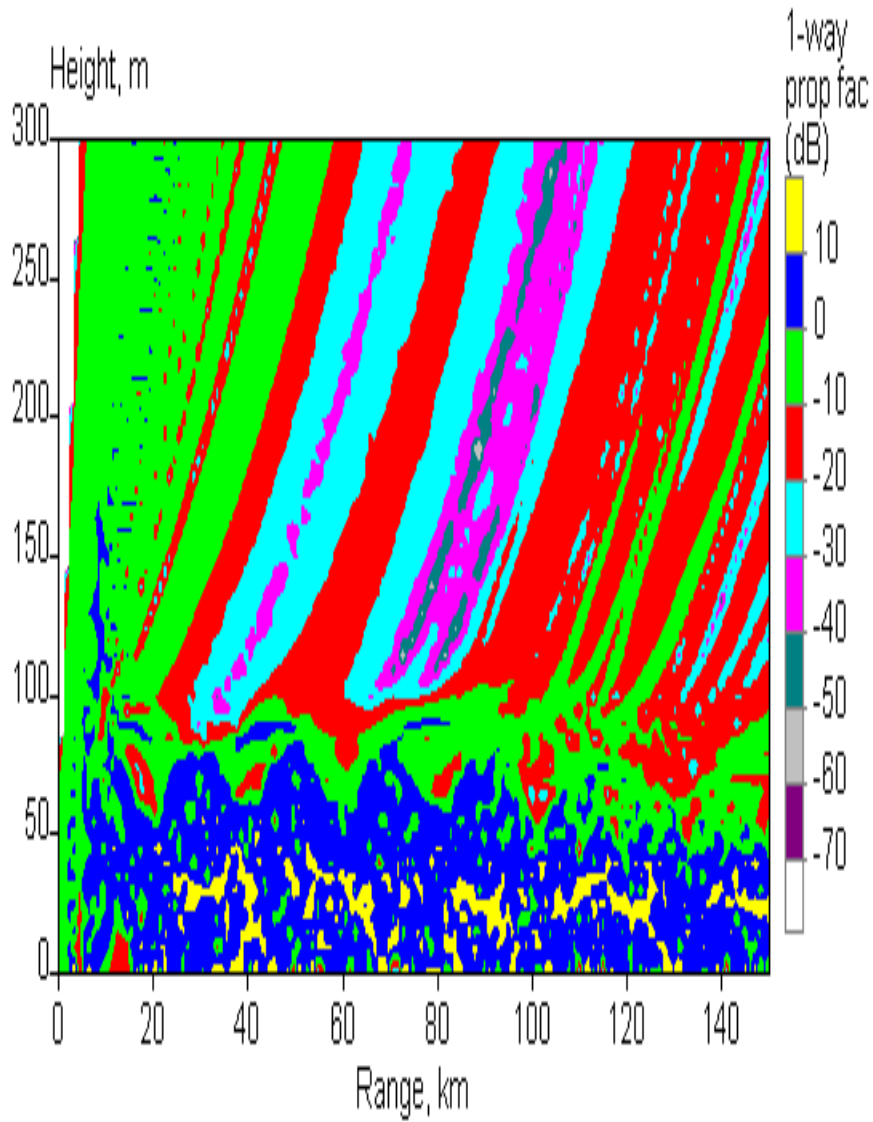
Figure 13: The 1-way propagation factor (dB) as a function of range (km) along the line $y = -54$ km at 1400 hr on the first day of a low wind run (Plant and Atkinson, 1999). The altitude is 330 m. A 10 GHz circularly–polarized radar was positioned 30 m above the surface at $x = 120$ km.
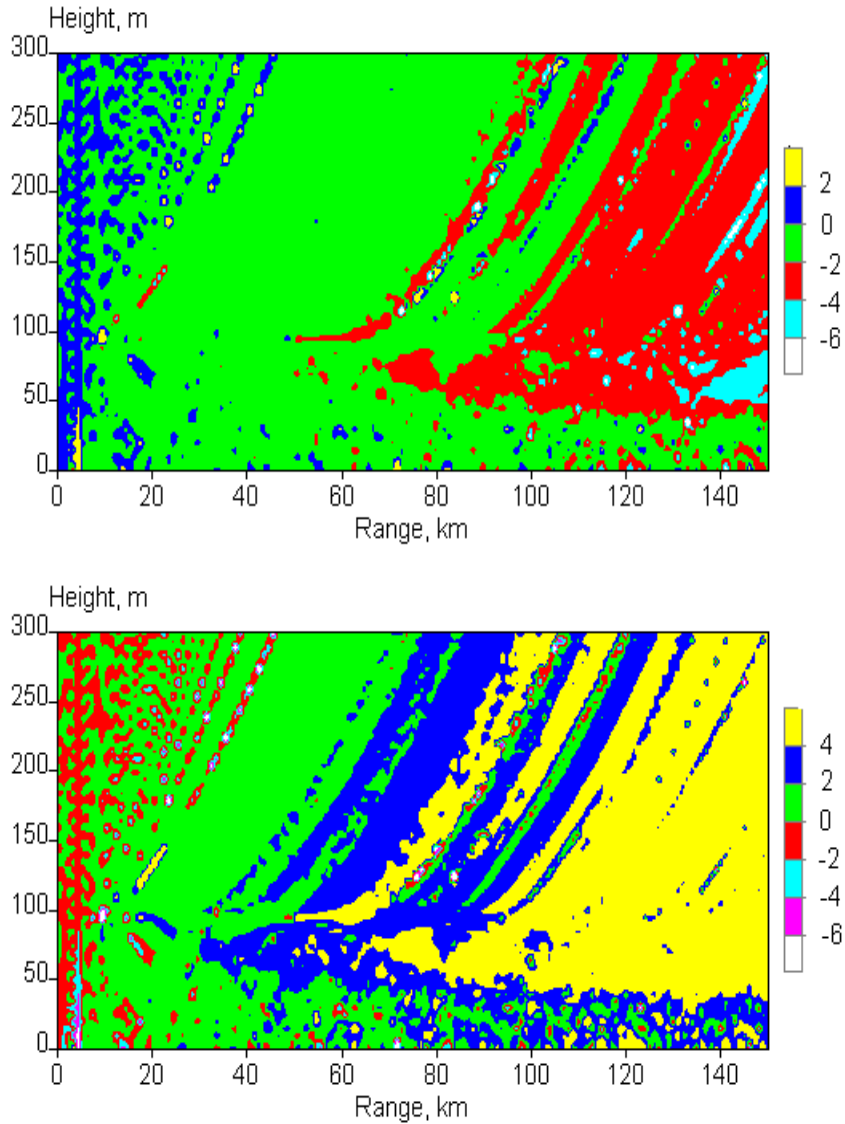
Figure 14: Differences between the path losses obtained using different polarizations. The radar path lay along the line $y = -54$ km at 1400 hr on the first day of a low wind run (Plant and Atkinson, 1999). A 10 GHz radar was positioned 30 m above the surface at $x = 120$ km. The upper plot shows the difference (dB) between circular and horizontal polarization; the lower plot shows the difference between vertical and horizontal polarization.
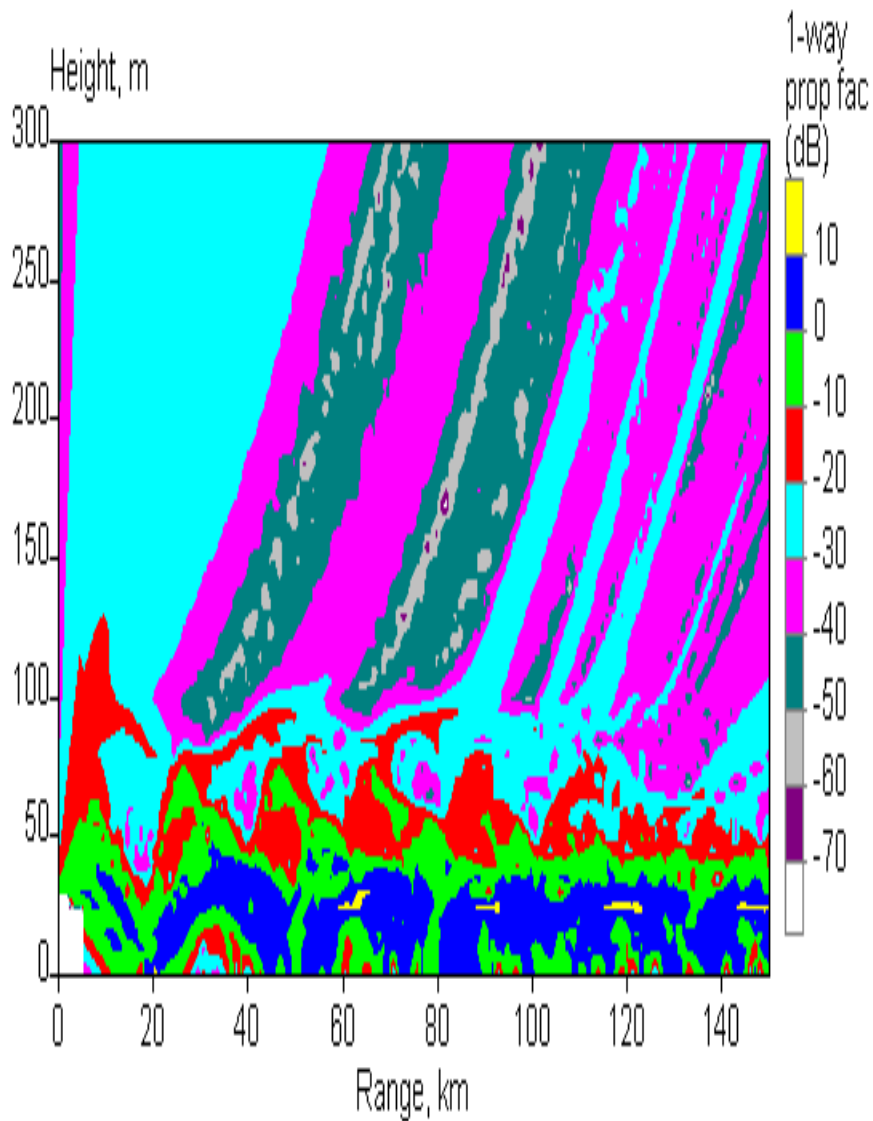
Figure 15: Coverage diagrams showing the 1-way propagation factor (dB) along the line $y = -54$ km at 1400 hr on the first day of a low wind run (Plant and Atkinson, 1999). A circularly–polarized radar was positioned 30 m above the surface at $x = 120$ km. The radar frequency was 3 GHz in the upper left plot, 1 GHz in the upper right plot, 300 MHz in the lower left plot and 100 MHz in the lower right plot.
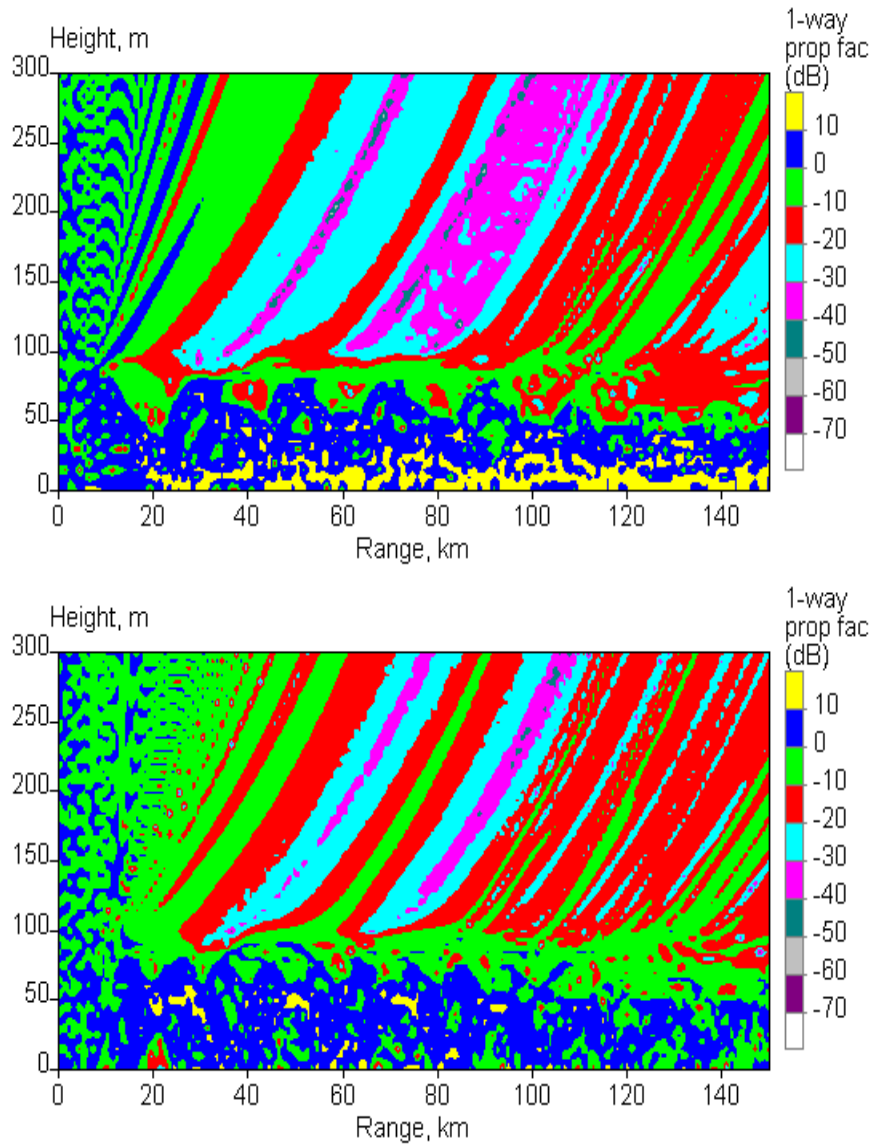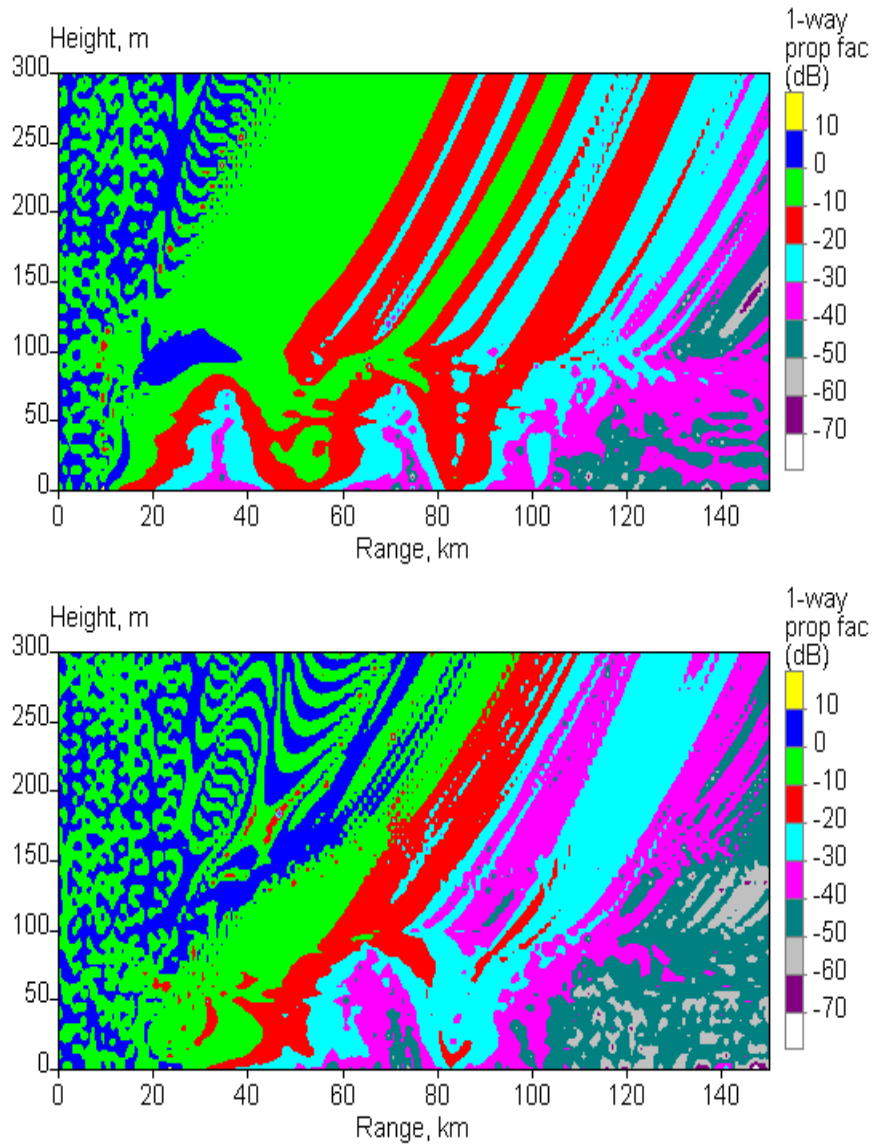
Figure 16: Coverage diagrams showing the 1-way propagation factor (dB) along the line $y = -54$ km at 1400 hr on the first day of a low wind run (Plant and Atkinson, 1999). A 30 GHz circularly–polarized radar was positioned 30 m above the surface at $x = 120$ km. In the upper diagram atmospheric absorption is taken into account; in the lower diagram absorption is neglected.
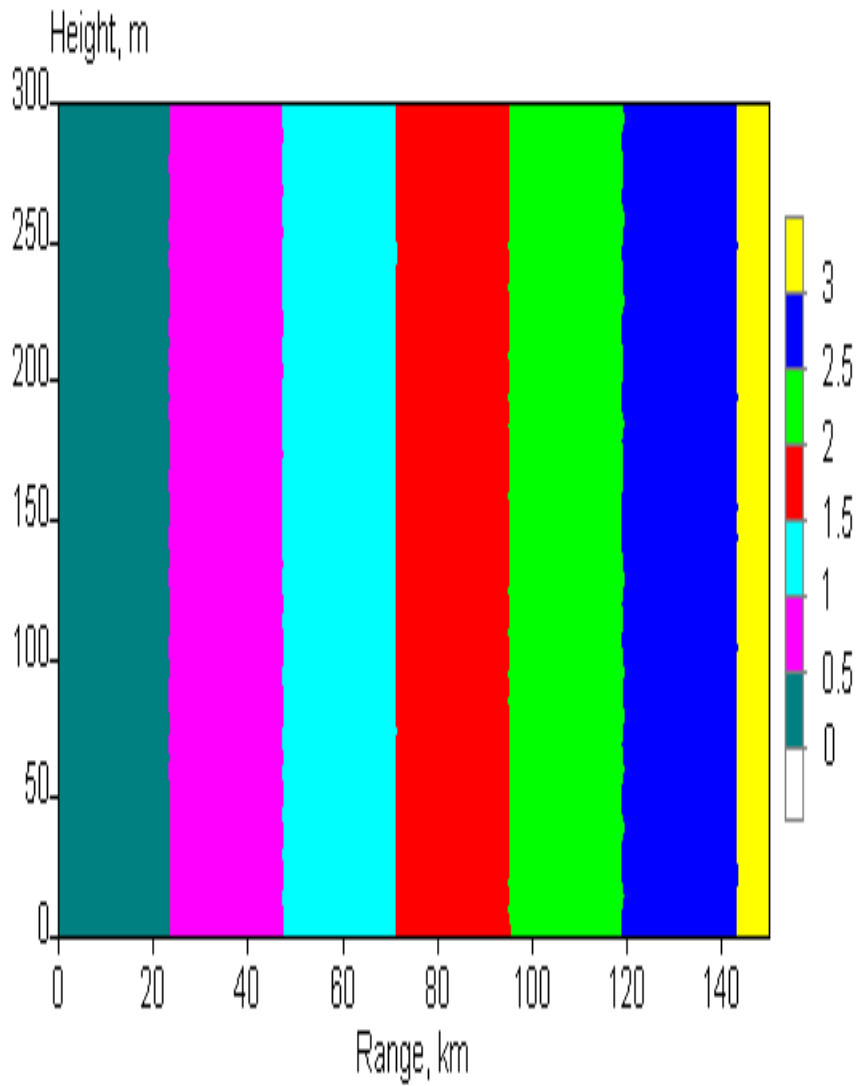
Figure 17: Difference in path loss (dB) between unattenuated and attenuated propagation. The radar path lay along the line $y = -54$ km at 1400 hr on the first day of a low wind run (Plant and Atkinson, 1999). A 10 GHz circularly–polarized radar was positioned 30 m above the surface at $x = 120$ km.

Figure 18: Difference in path loss (dB) between roughness–corrected and uncorrected propagation. The radar path lay along the line $y = -54$ km at 1400 hr on the first day of a low wind run (Plant and Atkinson, 1999). A 10 GHz circularly–polarized radar was positioned 30 m above the surface at $x = 120$ km.

Figure 19: A coverage diagram showing the 1-way propagation factor (dB) along the line $y = -54$ km at 1400 hr on the first day of a low wind run (Plant and Atkinson, 1999). A 10 GHz circularly–polarized Taylor antenna was positioned 30 m above the surface at $x = 120$ km.

Figure 20: A coverage diagram showing the 1-way propagation factor (dB) along the line $y = -54$ km at 1400 hr on the first day of a low wind run (Plant and Atkinson, 1999). A 10 GHz circularly–polarized cosecant–squared antenna was positioned 30 m above the surface at $x = 120$ km. The antenna was omni-directional for angles below $0.1°$.

Figure 21: Coverage diagrams showing the 1-way propagation factor (dB) along the line $y = -54$ km at 1400 hr on the first day of a low wind run (Plant and Atkinson, 1999). A 10 GHz circularly–polarized radar was positioned at $x = 120$ km. In the upper diagram the antenna was 10 m above the surface; in the lower diagram it was was 50 m above the surface.

53

Figure 22: Coverage diagrams showing the 1-way propagation factor (dB) along the line $y = -54$ km at 1400 hr on the first day of a low wind run (Plant and Atkinson, 1999). A 10 GHz circularly–polarized radar was positioned at $x = 120$ km. In the upper diagram the antenna was 100 m above the surface; in the lower diagram it was was 200 m above the surface.
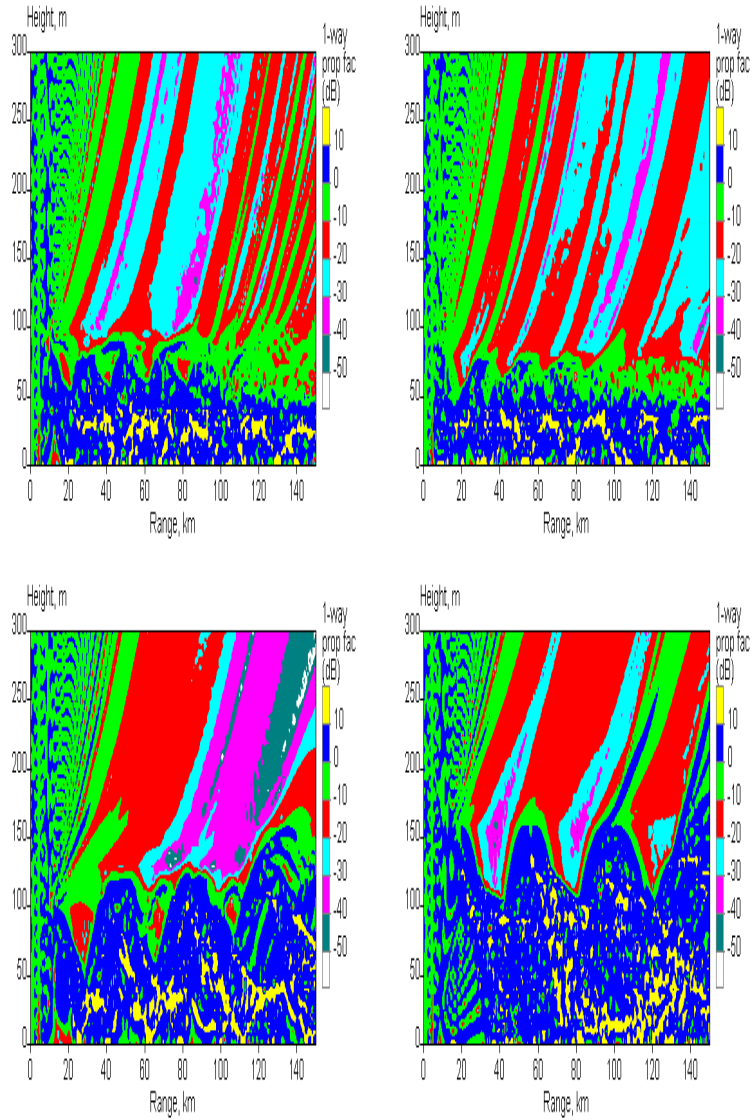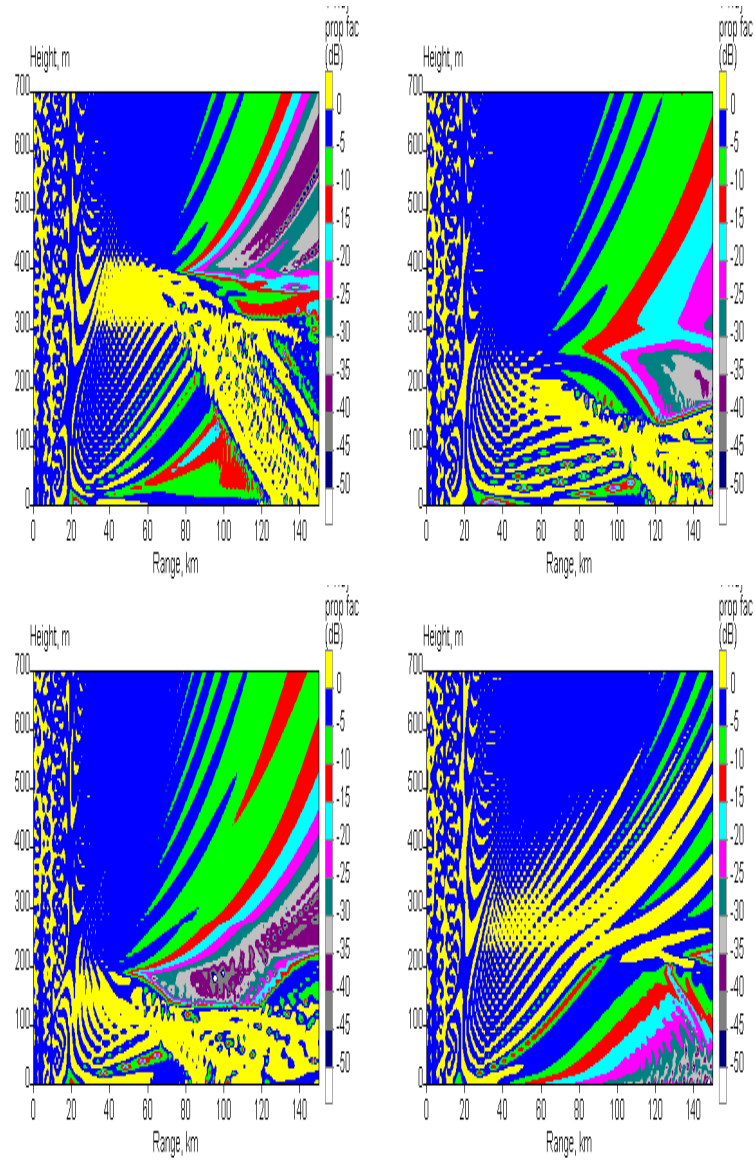
Figure 23: Coverage diagrams showing the 1-way propagation factor (dB) along the line $y = -54$ km for a low wind run (Plant and Atkinson, 1999). A 10 GHz circularly–polarized radar was positioned 30 m above the surface at $x = 120$ km. The time was 1400 hr on the first day in the upper left plot, 1800 hr in the upper right plot, 0200 hr in the lower left plot and 1400 hr on the second day in the lower right plot.
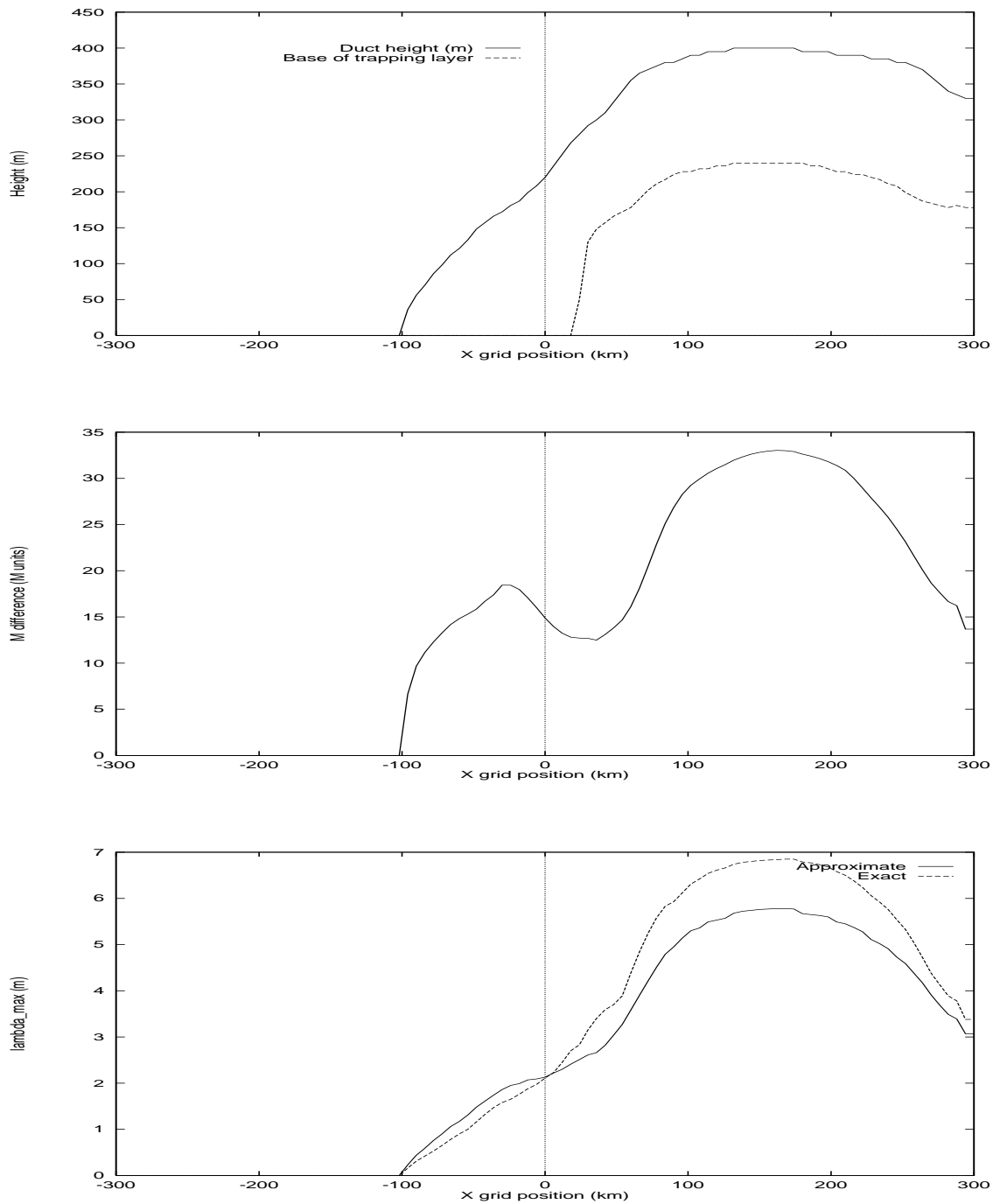
Figure 24: Duct parameters along the line $y = -54\,\mathrm{km}$ at $1400\,\mathrm{hr}$ on the first day of a high wind run (Plant and Atkinson, 1999). The upper plot shows the duct height (m) and the height of the trapping–layer base (m), the middle plot shows the modified refractivity difference across the duct (M-units) and the lower plot shows the maximum wavelength (m) of radiation that can be trapped by the duct. The lower plot shows the results from an exact calculation (Eq. 3) and from an approximate formula (Eq. 4).

Figure 25: Coverage diagrams showing the 1-way propagation factor (dB) along the line $y = -54$ km for a high wind run (Plant and Atkinson, 1999). A 10 GHz circularly–polarized radar was positioned 30 m above the surface at $x = 120$ km. The time was 1400 hr on the first day in the upper left plot, 1800 hr in the upper right plot, 2200 hr in the lower left plot and 0000 hr in the lower right plot.
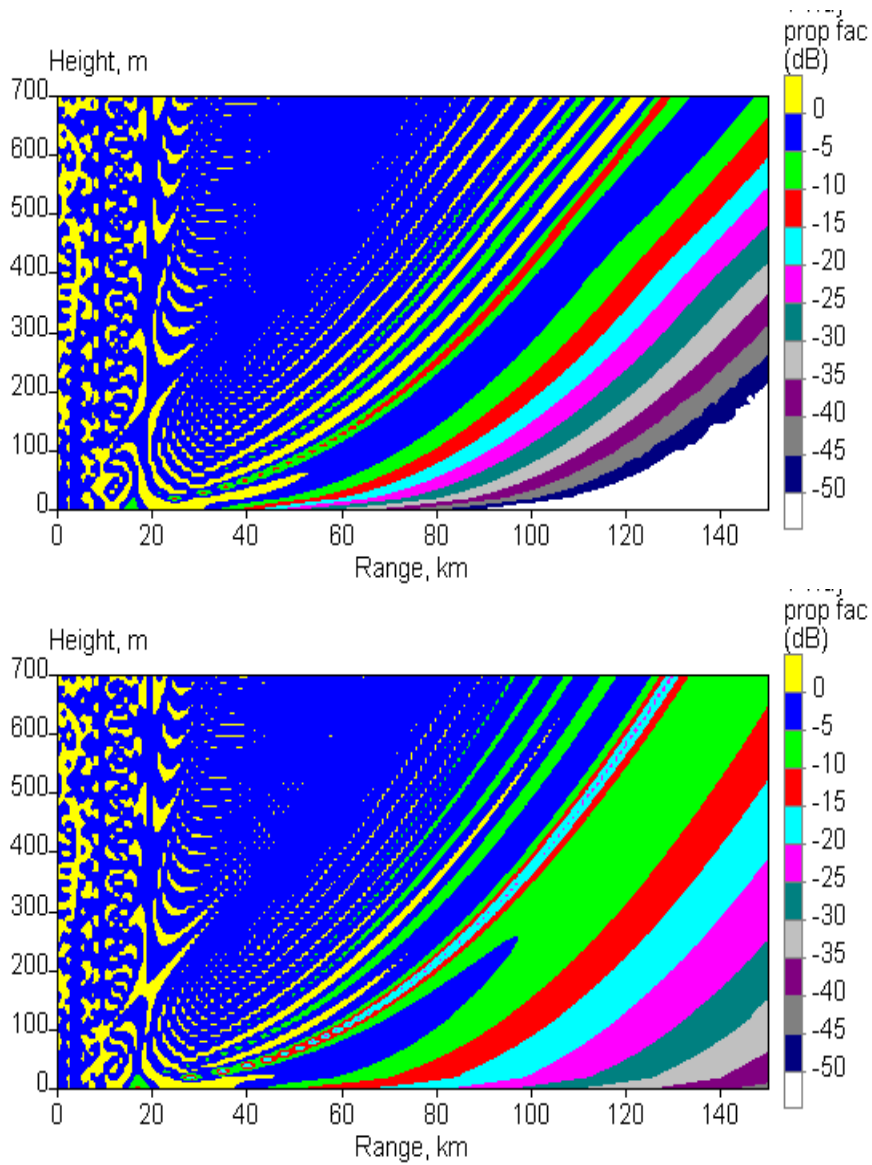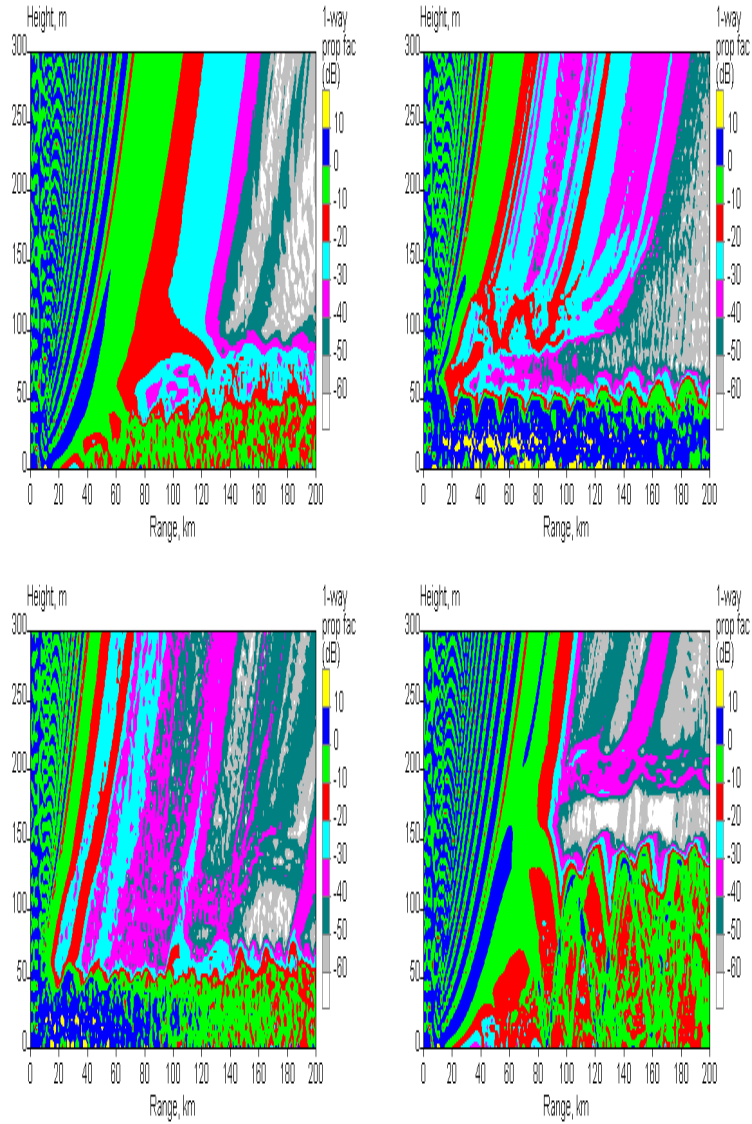
Figure 26: Coverage diagrams showing the 1-way propagation factor (dB) along the line $y = -54\,\text{km}$ for a high wind run (Plant and Atkinson, 1999). A 10 GHz circularly–polarized radar was positioned 30 m above the surface at $x = 120\,\text{km}$. The time was 0200 hr on the second day in the upper plot and 1400 hr in the lower plot.

Figure 27: Coverage diagrams showing the 1-way propagation factor (dB) along the line $y = -54$ km for a low wind run (Plant and Atkinson, 1999). A 10 GHz circularly–polarized radar was positioned 20 m above ground at $x = -120$ km. The time was 1400 hr on the first day in the upper left plot, 2000 hr in the upper right plot, 0200 hr in the lower left plot and 1400 hr on the second day in the lower right plot.
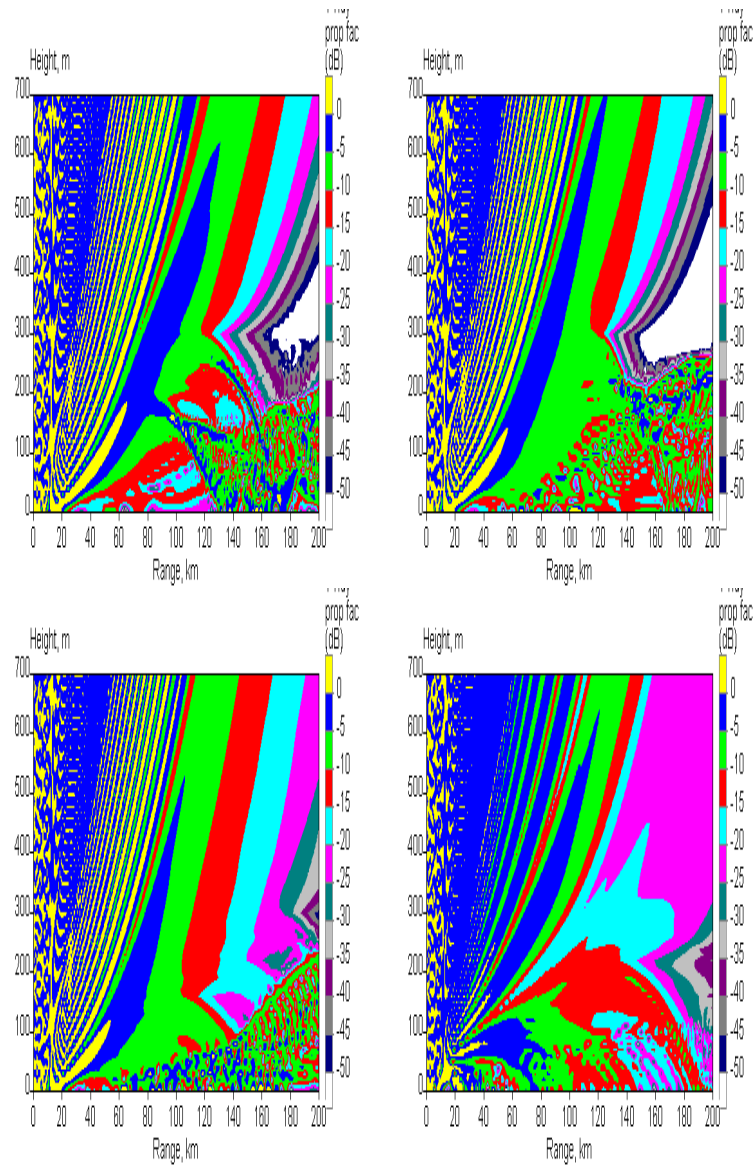
Figure 28: Coverage diagrams showing the 1-way propagation factor (dB) along the line $y = -54\,\text{km}$ for a high wind run (Plant and Atkinson, 1999). A 10 GHz circularly–polarized radar was positioned 20 m above ground at $x = -120\,\text{km}$. The time was 1000 hr on the first day in the upper left plot, 1200 hr in the upper right plot, 1400 hr in the lower left plot and 2000 hr in the lower right plot.
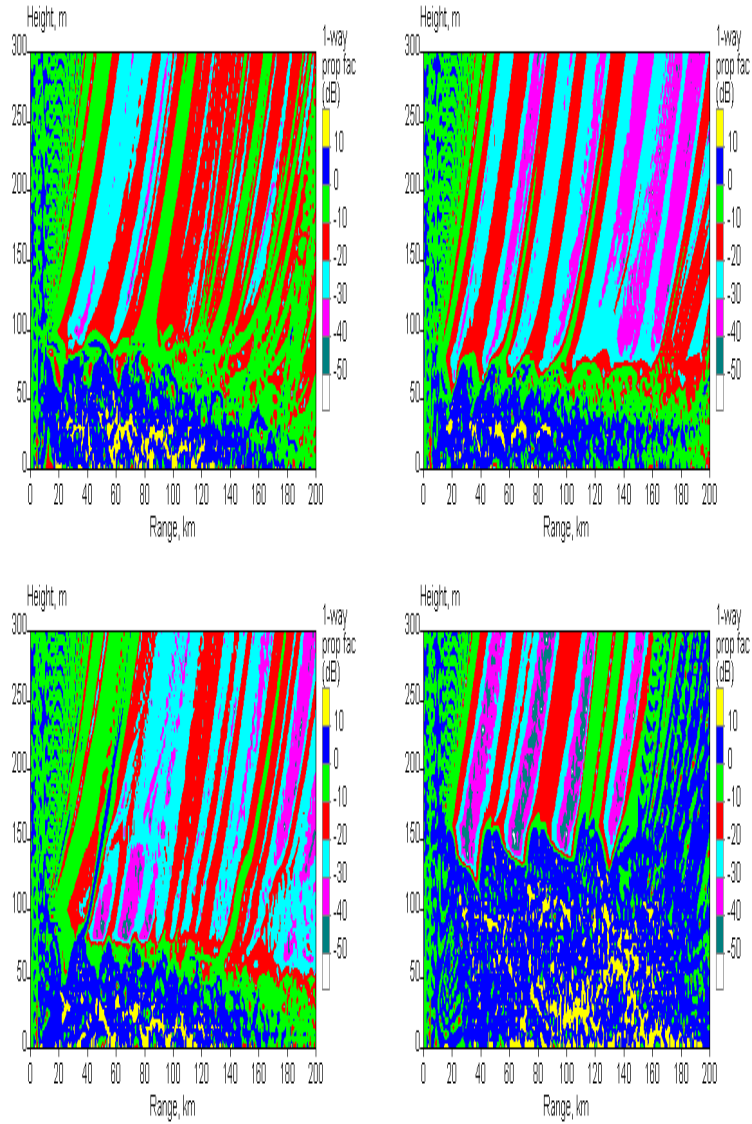
Figure 29: Coverage diagrams showing the 1-way propagation factor (dB) along the line $y = -54 \, \text{km}$, in the direction of decreasing x, for a low wind run (Plant and Atkinson, 1999). A 10 GHz circularly–polarized radar was positioned 30 m above the surface at $x = 80 \, \text{km}$. The time was 1400 hr on the first day in the upper left plot, 1800 hr in the upper right plot, 0200 hr in the lower left plot and 1400 hr on the second day in the lower right plot.
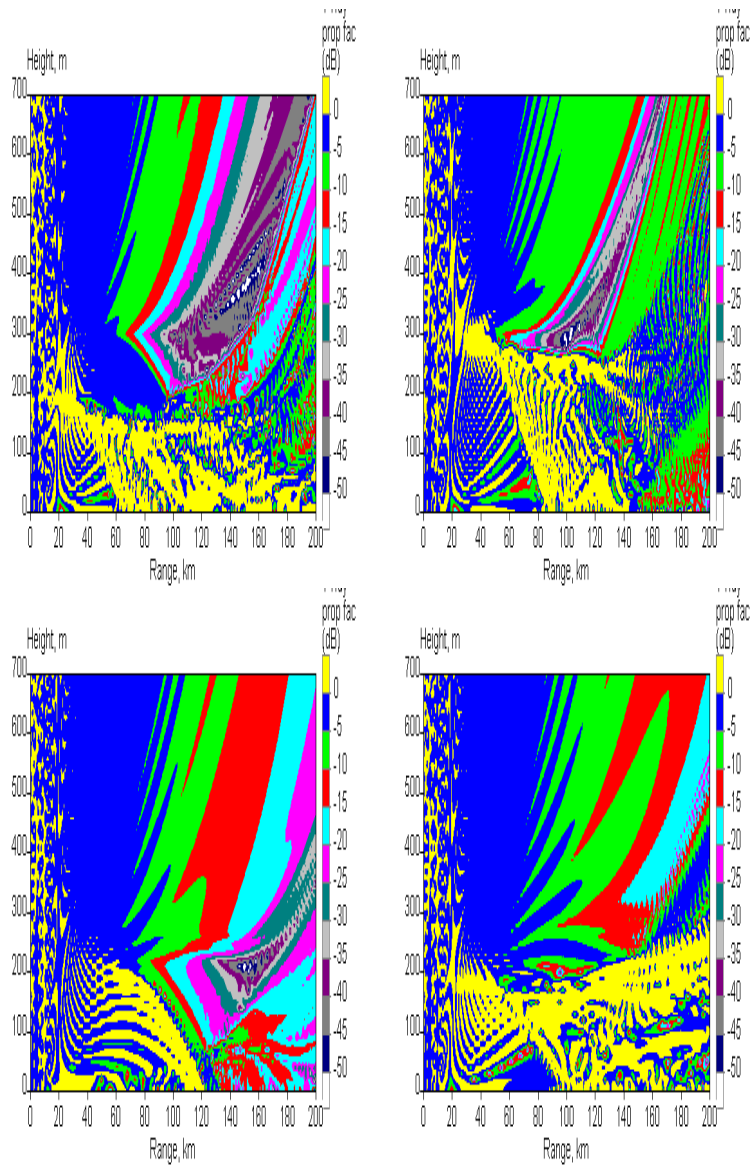
Figure 30: Coverage diagrams showing the 1-way propagation factor (dB) along the line $y = -54$ km, in the direction of decreasing x, for a high wind run (Plant and Atkinson, 1999). A 10 GHz circularly–polarized radar was positioned 30 m above the surface at $x = 80$ km. The time was 1000 hr on the first day in the upper left plot, 1200 hr in the upper right plot, 1800 hr in the lower left plot and 2200 hr in the lower right plot.
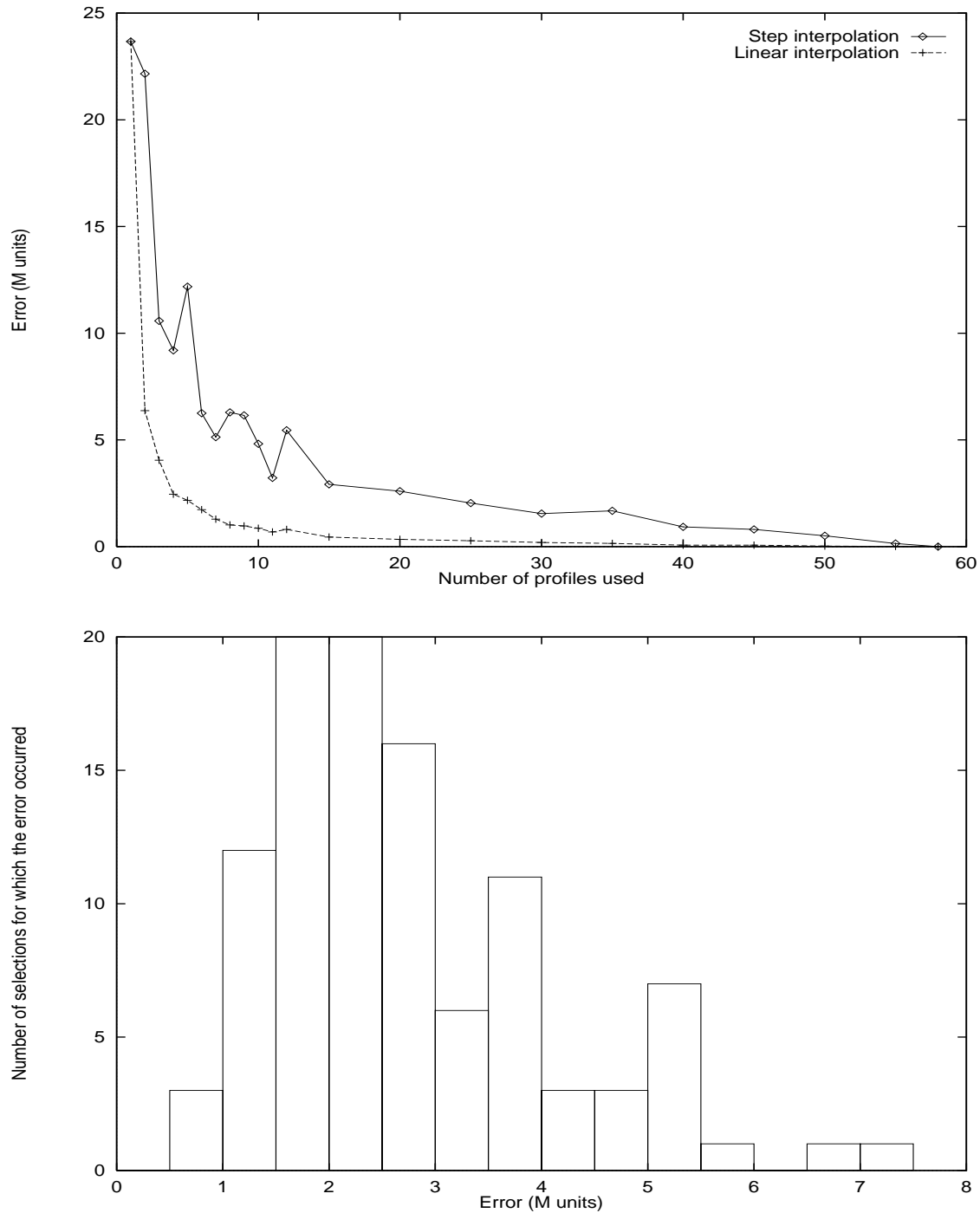
Figure 31: The upper plot shows the variation of the RMS error in the refractivity field with the number of profiles that are used in specifying that field. For a given number of profiles, 100 profile sets were chosen at random and the smallest error from those sets is plotted. The required refractivity field was that obtained at $1500\,\mathrm{hr}$ in a high wind run with a $3\,\mathrm{km}$ grid length (Plant and Atkinson, 2000) for $-120 < x < 50\,\mathrm{km}$, along the line $y = -54\,\mathrm{km}$. When ten profiles were used, the distribution of errors arising from the 100 randomly–chosen sets of profiles is shown in the lower plot.
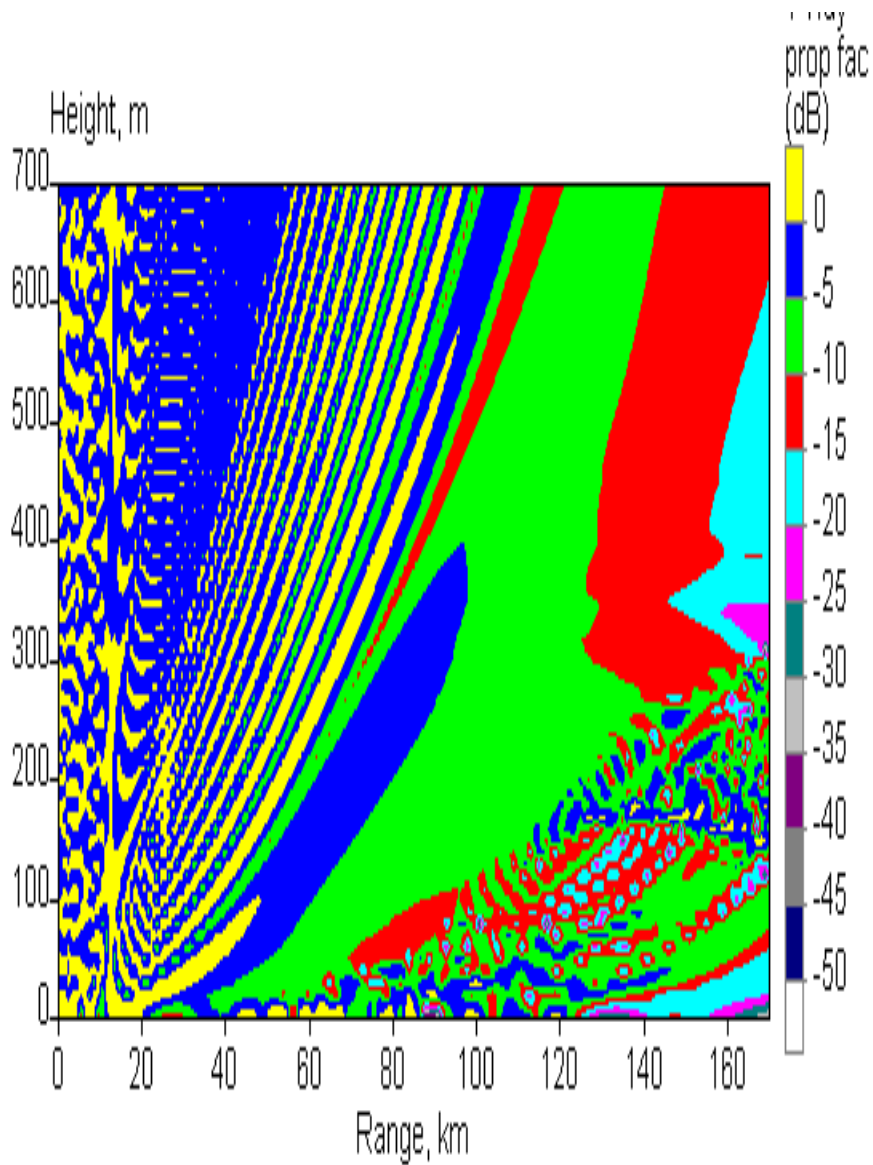
Figure 32: Coverage diagram showing the 1-way propagation factor (dB) along the line $y = -54$ km at 1500 hr during a high wind run (Plant and Atkinson, 2000). A 10 GHz circularly–polarized radar was positioned 20 m above ground at $x = -120$ km. The refractivity data used in TERPEM had an RMS error of 0.8 M-units.
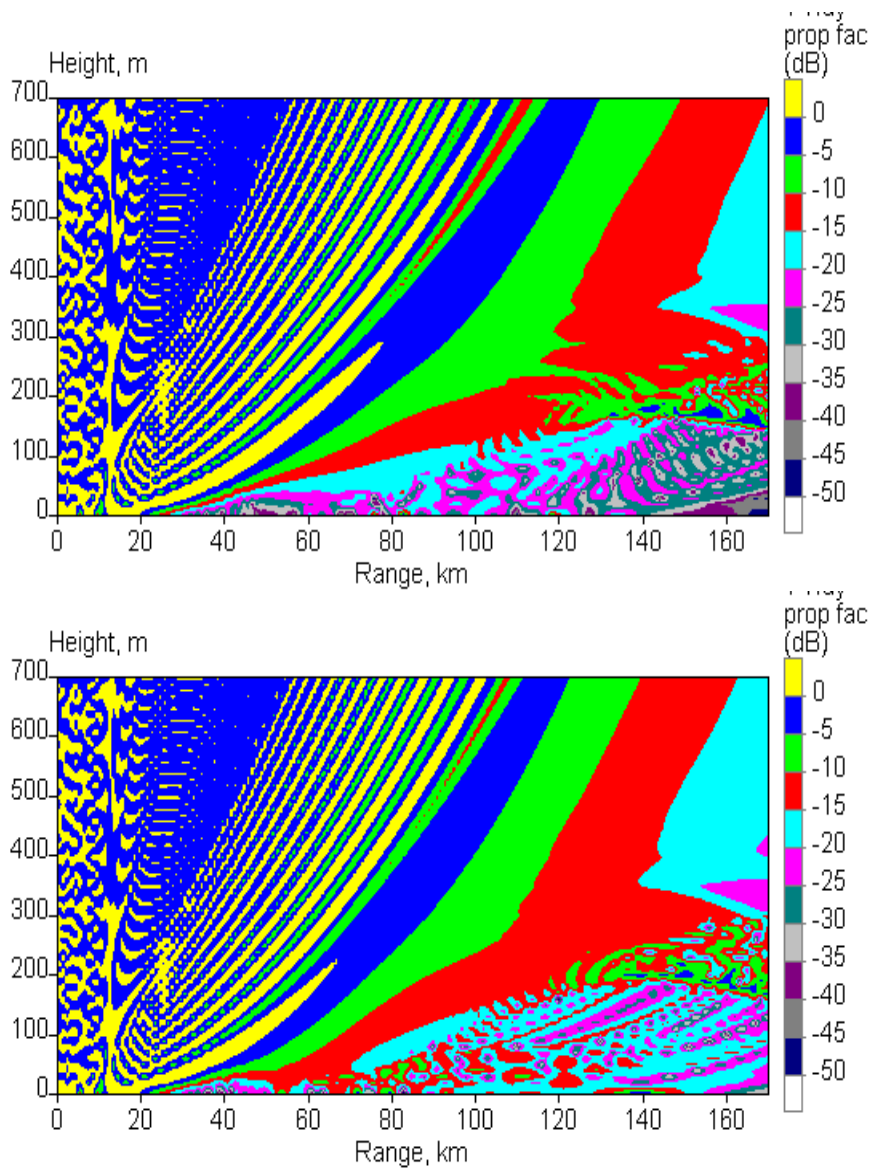
64

Figure 33: Coverage diagram showing the 1-way propagation factor (dB) along the line $y = -54$ km at 1500 hr during a high wind run (Plant and Atkinson, 2000). A 10 GHz circularly–polarized radar was positioned 20 m above ground at $x = -120$ km. In producing the upper plot, the refractivity data used in TERPEM had an RMS error of 1.5 M-units; in producing the lower plot, the error was 2.4 M-units.

A   Figures from Dockery (1988)

In this Appendix, we reproduce figures from Dockery (1988) for ease of comparison with the results of TERPEM runs described in Sec. 3. Some brief explanatory notes about these figures are given below.

- In Figs. 2 and 3 of Dockery (1988) the dashed lines give the results of calculations performed using a method described by Kerr (1951).

- Figs. 7 and 9 of Dockery (1988) are plotted on a 'gray–scale', using five bands to represent the power relative to free space. Each band represents an interval of $3\,\mathrm{dB}$, the top of the darkest band being set at $0\,\mathrm{dB}$. White areas on these figures represent signals weaker than $-15\,\mathrm{dB}$. Note that the same scheme has been used in producing the equivalent TERPEM figures for this report (Figs. 4 and 6) although, for clarity, coloured bands have been plotted here.

- In Fig. 8 of Dockery (1988) the dashed lines give the results of calculations performed using waveguide theory (Baumgartner Jr, 1983), representing propagation within the uniform duct as a sum of modes.

- The solid line plotted on Fig. 9 of Dockery (1988) indicates the duct depth as a function of range.

B   Figures from Brooks *et al.* (1999)

In this Appendix, we reproduce figures from Brooks *et al.* (1999) for ease of comparison with the results of TERPEM runs described in Sec. 4. The caption for the coverage diagrams on this page can be seen overleaf.